Simulation and Testing of a MU-MIMO Beamforming System

NAZYAR MEHDISHISHAVAN & ZONGHAN WANG
MASTER´S THESIS
DEPARTMENT OF ELECTRICAL AND INFORMATION TECHNOLOGY
FACULTY OF ENGINEERING | LTH | LUND UNIVERSITY

Simulation and Testing of a MU-MIMO Beamforming System

Nazyar Mehdishishavan, Zonghan Wang
na6138me-s@student.lu.se, zo4270wa-s@student.lu.se

Department of Electrical and Information Technology
Lund University

September 4, 2023

Abstract

Multi-User Multiple-Input Multiple-Output (MU-MIMO) technology has become increasingly important in the field of wireless communication due to its ability to highly increase the capacity and efficiency of wireless networks [1]. Beamforming, as a technique used in MU-MIMO systems, improves network performance by improving signal quality and reducing interference. With the emergence of 5G and beyond, the complexity of Advanced Antenna Systems (AASs) that perform beamforming has increased considerably. Consequently, testing the AAS before installation becomes vital to ensure the reliability and performance of the system. Meanwhile, the Butler matrix has gained significant attention as a passive device for efficient and cost-effective testing of the AAS and beamforming setup. Generally, the Butler matrix can be used in the Base Station (BS) of mobile networks to create beams towards the User Equipment (UEs).

In this thesis work, a method for beamforming tests based on channel reciprocity in MU-MIMO is studied. A beamforming setup in the laboratory using a Butler matrix to form beams is used before the BS is deployed in real-world scenarios. Based on the Sounding Reference Signal (SRS), which is received from the UEs, the BS estimates the channel for each UE separately and applies the appropriate weight matrix to determine beams towards the UEs.

The purpose of the study is to evaluate and validate the system for beamforming tests. Assessment is carried out in two parts. Taking everything into account, we first simulate a combination of directional signals using an Over The Air (OTA) test method. This simulation involves four UE positions. This approach enables us to verify the accuracy of the beam patterns generated by the system. Furthermore, it identifies side lobes that might be present in the beam patterns. Through these simulations, we can mitigate and reduce these side lobes, enhancing the overall quality of the testing process.

Secondly, measurements were performed in the Downlink (DL) and Uplink (UL) modes. In the DL measurements, the Physical Downlink Shared Channel (PDSCH) power and throughput of the UEs were measured for the setup in the laboratory. Subsequently, on the basis of our observation of low PDSCH power or low throughput values, we explored the root causes using UL measurements. The UL measurements involved recording the SRS traces. Our approach for obtaining SRS data, testing methodologies, precise data selection from log traces, and subsequently beam mapping algorithm are described in detail. The study includes a

i

comprehensive description of the methodology along with the corresponding results, ensuring a complete understanding of the process.

Acknowledgement

Popular Science Summary

The history of wireless communication began with the discovery of electromagnetic waves. The wired telephone system was introduced in around 1870, which paved the way for the later transition from traditional landline phones to superfast wireless connections. Wireless technology enables devices to communicate with one another while on the move. To make connections possible, transmitting and receiving antennas are used to send and receive electromagnetic signals, respectively. Traditionally, a single antenna is used at both the transmitter and the receiver, which involves a simple antenna process.

The advent of new generations of mobile systems has opened up new possibilities for antenna design. The size and power of the antennas and the way they communicate with each other have changed with the emergence of 5G technology. Unlike previous generations, 5G uses small cell structures and smart antenna systems to simultaneously send signals directly to several users. The improved hardware in 5G communication created the possibility of operating multiple devices in different locations at a higher speed.

As a key property of 5G, we can point to the Multi-User Multiple-Input Multiple-Output (MU-MIMO), which employs multiple antennas to transmit and receive signals. This technology enables communication of several devices with a single base station simultaneously. To make things clearer, it allows many people to use their smartphones simultaneously without disruption. As an example, MU-MIMO gives this opportunity to the audience in sports stadiums to share their experiences online without any disconnections.

For better utilization of the shared medium and the frequency band in 5G systems, beamforming technology is used. The application of MIMO antennas in beamforming and wireless technologies makes communications more efficient. Beamforming directs wireless signals precisely where they are needed, which leads to fast and clear communication even in crowded areas.

In recent years, the number of mobile users has increased significantly. Thus, with increased demand for reliable communications, Advanced Antenna Systems (AASs) are essential when implementing the aforementioned technologies, such as MU-MIMO and beamforming. These smart systems enable the transmission of signals without interruption within environments with high traffic.

Before applying the AASs to practical and real applications, it is essential to test them. Testing these antennas in real scenarios is complicated. Therefore, in

our thesis, we tested them in a laboratory setup in which the devices are connected by cables. In the laboratory, a Butler matrix is used to test the beamforming ability of the advanced antennas. The Butler matrix, a passive beamforming tool, helps us to assess the beamforming capability of these systems and how precisely they can guide signals in different directions.

One method of beamforming in 5G is called reciprocity-based beamforming. This beamforming method uses a special technique where devices send and receive signals along the same path and make communication clearer and more efficient. The Butler matrix is used for this process and ensures that these signals are sent and received in a way that minimizes confusion and that messages reach the intended place.

Before we start testing the advanced antennas with the Butler matrix, we need to double-check that the Butler matrix is doing its job correctly. It is like making sure that all the pieces of a device work perfectly together. So, we run dedicated tests. First, we measure the power of the signals that are transmitted from the base station to our devices. In this step, we check if the user receives enough power. We then measure special signals, transmitted from our devices to the base station. We make sure that the Butler matrix can take the signals from the advanced antennas and send them in the right direction with the expected power value. In this way, we can be sure that everything works smoothly when we use advanced and smart antennas in real deployments.

In this thesis project, our initial power measurements show that when we have one or two receivers, each of them receives enough power. However, with an increase in the number of receivers to four, our measurements reveal that some of the receivers cannot receive the expected power values. Consequently, we searched and identified the main cause of the problem.

Table of Contents

List of Figures

List of Tables

list of acronyms

5G	Fifth-Generation Mobile System
5G NR	5G New Radio
AAS	Advanced Antenna Systems
BLER	Block Error Rate
BS	Base Station
CCN	Cellular Coaxial Network
CSI	Channel State Information
DU	Digital Unit
eMBB	Enhanced Mobile Broadband
EVM	Error Vector Magnitude
FFT	Fast Fourier Transform
gNB	5G Next Generation Base Station
HSPA	High Speed Packet Access
IFFT	Inverse Fast Fourier Transform
LTE	Long Term Evolution
MIMO	Multiple-Input Multiple-Output
MU	Multi-User
OFDM	Orthogonal Frequency Division Multiplexing
OTA	Over The Air
PA	Planar Array
PDSCH	Physical Downlink Shared Channel
PRB	Physical Resource Block
PUSCH	Physical Uplink Control Channel

RB	Resource Block
RCE	Relative Constellation Error
RF	Radio Frequency
SCG	Sub Carries Group
SINR	Signal to Interference plus Noise Ratio
SNR	Signal to Noise Ratio
SRS	Sounding Reference Signal
SSB	Synchronization Signal Block
STP	System Test Plant
SU	Single-User
TDD	Time Division Duplex
UE	User Equipment
ULA	Uniform Linear Array
UPA	Uniform Planar Array

Introduction

1.1 Motivation and background

With the development of wireless communication systems in recent years, the demand for higher capacity systems increased. To enhance communication performance and quality, a Multiple-Input Multiple-Output (MIMO) system with multiple antennas at the transmitter and receiver sides was already introduced in High Speed Packet Access (HSPA) and Long Term Evolution (LTE). However, with the growing demand for even higher data rates and further increases in the number of users, the conventional MIMO technique was no longer sufficient. At this point, Multi-User Multiple-Input Multiple-Output (MU-MIMO) was introduced. In contrast to traditional systems where communication with each device occurs in separate time/frequency resources, MU-MIMO is a technology that enables multiple UEs to simultaneously communicate with a single BS over the same time-frequency resource. The key benefit of MU-MIMO in the context of 5G is its role in significantly increasing network capacity. Traditional wireless systems often struggled when numerous devices tried to communicate simultaneously.

In addition to being a MU-MIMO technology, beamforming is a signal processing technique that plays a vital role in the improvement of wireless communication systems. It shapes and directs the radiation pattern of transmitted or received signals to maximize the strength of the signal at a desired location, leading to increased throughput. By focusing the signal energy toward the intended UE, beamforming significantly improves signal quality and overall network performance.

To fully exploit the potential of these two cutting-edge technologies, Advanced Antenna Systems (AAS) have received significant attention. AAS can be divided into two categories of adaptive arrays and switched beam systems [2]. In the first type, BS can effectively reject interference. It is a complicated method that requires a lot of signal processing. Although the second type is not as efficient as adaptive arrays, it is simple and less expensive [3]. A system utilizing beam switching generates numerous beams and then chooses the most suitable beam based on the strongest signal level. A Butler matrix can be used as a beamforming device similar to the switched beam system and can be effective in creating the multibeam characteristics of antennas [4], which is the ability to create multiple separate beams simultaneously. The Butler matrix serves as a mechanism that

facilitates efficient communication between multiple antenna arrays and the main transceiver unit. The Butler matrix is a bidirectional component and can be used in both UL and DL scenarios. It is made up of power dividers, phase shifters, and crossover connections. The Butler matrix can apply constant phase differences on antenna elements and the beams created by the Butler matrix are fixed beams in fixed directions. An NxN Butler matrix consists of N input and N output ports that feed N antennas where all the paths between the input and output ports are equal in length [3].

To have an efficient connection with each UE, the BS must have information about the channel. Reference [5] implements the DL MU-MIMO beamforming using channel reciprocity in a Time Division Duplex (TDD) scenario. Specifically, the BS array utilizes the channel estimation derived from the UL pilots sent by the devices to understand the channel characteristics in both transmission directions.

In [6], a similar topic was studied. The performance evaluation of a beam simulation system that studied a codebook-based beamforming system using the Channel State Information Reference Signal (CSI-RS) was considered. Different configurations and precoding schemes were applied, and the measurements results were compared with simulation results. Similarly, we study the same system setup from different angles, employing the Sounding Reference Signal (SRS) for channel estimation and beamforming application.

In [7], the focus is on evaluating the beamforming capabilities of the AAS. The study examines how the AAS facilitates advanced beamforming and MIMO techniques to enhance network capacity. The AAS configuration discussed in this research is identical to the one employed in our project; however, it varies in terms of size.

Figure 1.1 gives a graphical overview of how several antenna elements can change the direction of the wavefront [8].
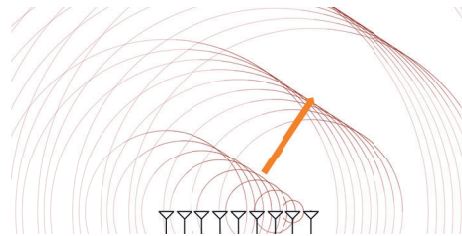
Figure 1.1: Directing the beam using multiple antennas

When it comes to beamforming and the Butler matrix as a beamforming device, there are some uncertainties to be considered. In real-time scenarios, in which beams are shaped toward the UEs, an important issue is how much separability is needed to have the best isolation between beams toward each UE. In the beamforming process, several antenna elements are used to control the direction of the wave. By changing the individual phase of each antenna element, it is possible to direct the beam in the desired direction, without any physical movement of the antennas.

Reference [9] highlights that testing how well radios work has become more complex because now companies have to test the AAS while considering the beamforming network and antenna arrays. The 5G testing field is still in its early stages, which signifies the potential for research on efficient measurement and testing methods.

Reference [10] considers hybrid beamforming as we use it in our setup. This paper uses hybrid beamforming and aims to develop a tool for testing planar arrays. The investigation is also based on the measurement data and test results, which is the same as our beamforming study. However, there are two main differences. First, it considers an OTA channel and aims to compare the measurements with an ideal channel model, whereas in our setup, we only use cables. Second, that investigation focused on how the correlation error in the antennas changes with the antenna setup; in our case, we aim to explain the mismatch in the relationship between the Butler matrix and the expected beamforming performance.

In [11], the researchers employ a Multi-Probe Anechoic Chamber (MPAC) to test 5G Millimeter-Wave (mmWave) cellular communications without wires and investigate the effect of phase noise on the Power Angular Spectrum (PAS). The authors also provided a method to estimate the beamforming directions in imperfect scenarios.

In [12], a test bench was created to evaluate the effectiveness of Digital Beamformer Networks (DBFN) for transmitting signals through cables. In our test system, the Butler matrix also consists of hybrid couplers and cables that work as phase shifters and attenuators. The cable network shares some similarities with our setup. The amplitude and phase change for each RF input signal is calculated and controlled by a computer on paper. However, in our system, only beam weights are controlled by the Digital Unit (DU) digitally, and the phase shifters in the Butler matrix work as analog devices.

In summary, to apply beamforming in the real world, it is essential to test the efficiency and accuracy of the system in a laboratory environment to verify the beam resolution and received power.

1.2   Thesis objectives

- The first objective of the thesis is to simulate the lab setup for MU-MIMO beamforming for different UE combinations. On the basis of the simulation in Matlab, the theoretical phase shift vectors generated by the Butler matrix and multiple UE beamforming directions supported by AAS should be verified.

- By analyzing the system's performance under multiple UE scenarios, by increasing the number of UEs, we aim to find the start point when the Butler matrix starts showing imperfect measurement results. Searching for the root of the problems will provide valuable insights into designing and implementing efficient MU-MIMO systems in real-world applications.

- Another important issue that needs to be considered in the Butler matrix beamforming system is how the mismatches of the Butler matrix affect the beam directions. By considering the mismatches in the phase shifts applied

on the antennas, a method should be given to estimate the beamforming directions based on the measurement data.

- As stated above, the system tested in the laboratory must be reliable enough to be applied to practical situations. Hence, the subsequent objective of the project is to conduct a performance evaluation of the MU-MIMO system in a laboratory setup and investigate the effectiveness of the Butler matrix in mapping the beams from the 64tx AAS radio towards 16 UE directions. All the connections between the UE and the BS in the laboratory were established using cables. Consequently, the evaluation of beam mapping capability cannot be conducted considering only power. A new measurement method should be designed to verify the effectiveness of the Butler matrix and show the error when the measurement result is not as expected.

- To evaluate the performance of the lab system, theoretical values and measurement data are compared to calculate the error margin of the system. Equally important is to investigate how these errors affect the system performance.

1.3   Approach and methodology

- In the simulation part, the simulation starts from a small 4×4 Butler matrix and ends with a large 32×16 Butler matrix. Then the AAS is simulated with the help of Matlab. Theoretical fixed beamforming directions were derived through calculations. After the simulation, we select four vectors representing four directions in the Butler matrix and apply the vector to the AAS simulation. Verification can be achieved by visualizing the 3D beam pattern for multiple beamforming directions.

- In the measurement part of the project, measurements are conducted from two different aspects. Initially, we measured throughput, BLER (Block Error Rate), EVM (Error Vector Magnitude), and received power for each UE in a MU-MIMO scenario in DL to check the possibility of undesirable and unforeseen values. Another approach in this thesis measurement is using the channel estimation information from SRS for reciprocity-based beamforming in MU-MIMO. Considering reciprocity, the radio channel has the same characteristics in UL and DL. Therefore, we can use the uplink channel estimation for DL transmission. This measurement can be performed in a DU after FFT. By processing the beam weights included in channel estimation, we can obtain phases added to antenna elements by the Butler matrix. As a part of this step, we search for the reasons why the BS does not receive the proper SRS signals in some of the test cases.

- For the beam analysis, two methods are adopted, Taylor expansion and polynomial curve fitting, to estimate the beamforming direction in horizontal and vertical directions with the measurements. Leakage and noise are

considered and checked for their influence on beam mapping directions.

- Taking into account the theory and simulation aspects, the mismatches between the phase vectors applied on the antennas and those provided by the Butler matrix are visualized. The errors are calculated and the influence on the received power and EVM of each UE, as well as the beamforming direction, is investigated with the help of DL measurement. The performance of the system is evaluated based on the received power, EVM, and beam mapping directions.

1.4   Thesis organization and outline

Chapter 2 focuses mainly on the background and provides the context and theoretical explanation of the devices and techniques employed in this project. This chapter offers a comprehensive overview of the principles and application of the MU-MIMO, the beamforming technique, the Butler matrix, and the AAS. Chapter 3 describes the lab setup in detail and illustrates the application of the topics in the project framework. Chapter 4 provides an analysis of the simulation methodology and outlines the simulation results for different configurations. In Chapter 5, the measurement results of the laboratory setup and the log traces are provided. Chapter 6, analyzes and discusses the results obtained from the measurements and compares them comprehensively with the theoretical values. Moreover, methods for refinement and troubleshooting in measurements are presented. The final chapter, Chapter 7, gives the summary and conclusion of the project and provides possible future research topics.

Background and Techniques

2.1 MU-MIMO

MIMO technology has been used in modern and conventional communication systems for many years. It enables high data rates by deploying several antennas on both the transmitter and receiver sides. Spatial multiplexing, a core technology in MIMO systems, utilizes multiple antennas to create multiple independent paths, which can be used to transmit independent data streams between two ends of the communication system to increase throughput. In the new generations of communication networks (5G and beyond), there is a need to accommodate more UEs, and the BS needs to be in contact with more than one UE simultaneously, utilizing the same time-frequency resource. For this purpose, the MU-MIMO technique was proposed, and it became an important concept in 5G. MU-MIMO is a promising approach that responds to the demand for higher network capacity and data rate of the communication link, since it enables Spectral Efficiency (SE) and Energy Efficiency (EE) [13]. MU-MIMO uses spatial multiplexing techniques to transmit independent data streams, as each wireless channel can have different properties for different spatial paths. Spatial multiplexing can be implemented using the beamforming technique illustrated in Figure 2.1.
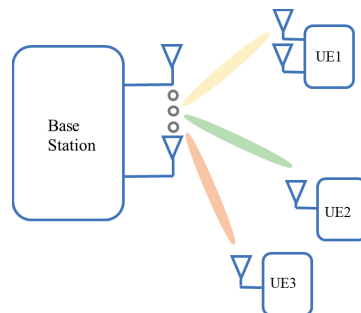
Figure 2.1: MU-MIMO in 5G New Radio (NR)

2.2   Multi-beam antenna and beamforming

Beamforming enables the concentration of the antenna radiation towards the intended UE which increases the Signal to Noise Ratio (SNR) and eliminates or reduces the level of interference in the system. Beamforming can be implemented with conventional multiple antenna arrangements or multibeam antennas. This kind of antennas can create multiple beams that can be combined into one or several shaped beams to cover a specific area and concentrate maximum power in the main lobe, which leads to less power in the side lobes that are unwanted in the beamforming process. As some key advantages of the multibeam antenna technology, we can point to:

- Increased network capacity: Multibeam antennas can initiate multiple simultaneous connections with different UEs in their coverage area, using the same time-frequency resource. This is made possible by the same time-frequency resource being reused by multiple beams serving different UEs.

- Enhanced spectral efficiency: Employment of the multibeam antenna technology makes it feasible to use the same time-frequency resource for different beams without considerable interference. Consequently, more efficient utilization of the available spectrum will improve spectral efficiency.

- Higher data rate: Increased network capacity and spectral efficiency will result in a higher data rate that is extremely vital in 5G networks.

- Improved coverage: By actively adjusting the beamforming parameters, the multibeam antenna can focus the energy towards a specific UE or area, which can provide more coverage and signal strength compared to the traditional single-beam antennas.

In Section 2.3, we will discuss the formation of multibeam antennas using the Butler matrix in AAS.

2.2.1   Reciprocity-based beamforming

As discussed above, beamforming is the ability to direct the antenna radiation through the radio channel towards the intended UE. Therefore, beamforming requires Channel State Information and synchronization. Reciprocity-based beamforming is a technique that exploits the reciprocity property of the wireless channel to direct the beam in time division duplex (TDD) scenarios where the system uses the same frequency bands at different times for uplink (signal transmitted from the UE toward the BS) and downlink (signal transmitted from the BS toward the UE) transmissions. The reciprocal channel has the same characteristics for both UL and DL channels. The SRS-based beamforming technique applies the beamforming weights for DL by using the channel estimation information based on the SRS. SRS is transmitted by UEs in the UL, and the BS estimates the channel and schedules PDSCH, which is the main physical channel used for unicast data transmission for multiple UEs using the same frequency and time domain resource blocks [14]. Figures 2.2(a) and 2.2(b) illustrate the DL beamforming technique for MU-MIMO.

(a) The SRS transmission in UL   **(b)** The PDSCH power transmission in DL
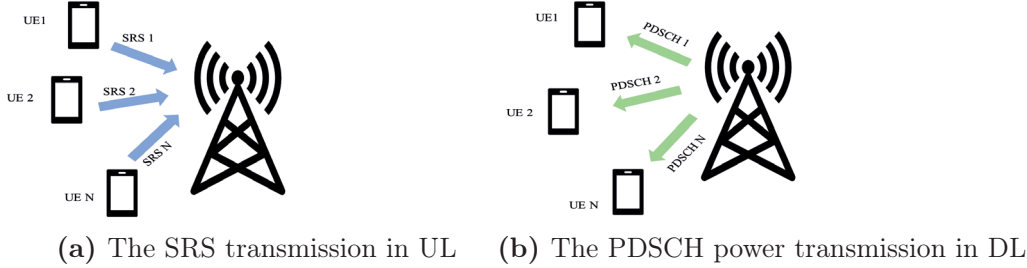
Figure 2.2: Downlink MU-MIMO beamforming using
uplink channel estimates

Assuming reciprocity of the channel, the BS can then use the UL information
to calculate the optimal beamforming vector for the DL beamforming. Unlike tra-
ditional beamforming techniques that require detailed feedback from the mobile
device, reciprocity-based beamforming using the SRS does not require feedback,
reducing the system's overhead and complexity. Enough number of antennas in
the BS enables more resolution in the directed beams, while UEs are subjected to
lower interference from one another. SRS-based beamforming provides significant
improvements in system performance, including increased capacity, spectral effi-
ciency, and energy efficiency, making it a promising technique for next-generation
wireless communication systems.

2.2.2   The SRS structure

The SRS is a predefined signal with known characteristics transmitted by the
mobile device and is designed to provide information on the channel response
to BS. The SRS in 5G has different configurations and parameters depending
on the specific use case and deployment scenario. These parameters include the
frequency and time resources allocated to the SRS, the number of antenna ports,
and the transmission periodicity. The BS is responsible for providing the UE with
the SRS configuration, which can vary based on the cell's conditions and traffic
demands. The SRS transmission can be periodic or nonperiodic based on the UL
configuration. The duration of the SRS in a slot is one, two, or four consecutive
OFDM symbols, and it is located in the last six symbols in the slot. The SRS is
transmitted within every Nth subcarrier and N can be two or four and is called
a combination number. Figure 2.3 depicts the key parameters of SRS resource
allocation [15].

The SRS resource shows the length of the SRS in the time domain and $K_{TC} \in$
$\{2, 4\}$ corresponds to the combination number. $N_{symb} = \{1, 2, 4\}$ gives the number
of SRS symbols in one slot. The number of the first symbol occupied by SRS is
specified by the I_{offset} value that can be between 0 and 5. The SRS helps in
the reciprocity-based DL precoding in MU-MIMO. The SRS received in the BS
is compared with the known reference signal, and parameters such as path loss,
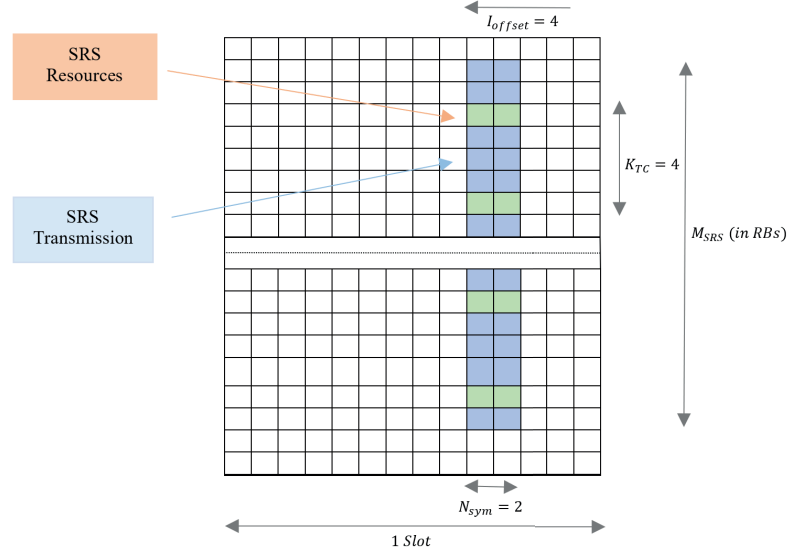
Figure 2.3: SRS resource allocation

propagation delay (phase delay), and received signal strength can be evaluated to gain insight into the radio environment.

2.3 The Butler matrix

The Butler matrix is a passive beamforming device that is used to distribute signals among multiple beams with high efficiency. It can be built in different variants, including 2×2, 4×4, 8×8. The Butler matrix consists of a series of power dividers and phase shifters.

In MU-MIMO systems, a Butler matrix can be used to efficiently distribute signals among multiple antennas, allowing multiple UEs to transmit and receive data separately. By using a Butler matrix as a bidirectional device that exploits channel reciprocity in an MU-MIMO system, each UE can be assigned a unique beamforming vector, which can be adjusted by the phase shifters in the Butler matrix to minimize interference among the UEs. The Butler matrix can also be used to adjust the power level of each UE's signal to achieve the desired signal-to-interference-plus-noise ratio (SINR) at the receiver. In addition, a Butler matrix can be used to implement spatial filtering techniques, such as nulling, to further reduce interference and improve system performance. Generally, using the Butler matrix in an MU-MIMO system can be an effective way to improve the capacity, spectral efficiency, and data rate of the system, which makes the Butler matrix a useful tool for next-generation wireless communication systems. Figure 2.4 shows the schematic of a conventional Butler matrix.
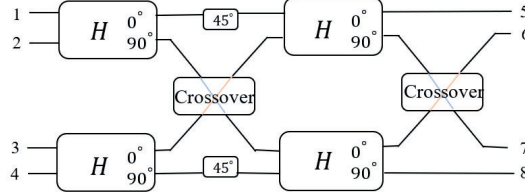
Figure 2.4: Traditional Butler matrix schematic

2.4 Antenna array structure

In 5G networks, with an increasing number of UEs and a higher capacity demand, a method is needed to increase capacity while reducing the operating expenses of the system. A promising method is to use a large number of antennas in the BS. The previous sections illustrate the importance of multibeam antenna technologies such as beamforming in high-frequency RF applications by highlighting their ability to direct the beams. This kind of antenna array deploys multiple antenna elements to control the wave-front direction. Inside the array structure, elements are placed at an equal distance from each other, usually half wavelength. Different directive patterns can be created by varying and controlling the phase of each antenna element in the array. A sequence of weights representing applied phase shift difference from one antenna to the one adjacent to it will generate a beam towards one direction. Phased array antennas are the typical type of antenna arrays for beamforming and they can be built in three configurations, i.e., linear, planar, and frequency scanning arrays. The linear and planar array configurations will be described in detail below.

2.4.1 Uniform Linear Array (ULA)

Figure 2.5 depicts a uniform linear antenna array and how it forms and directs a beam in a specific direction [6]. Each dot represents an antenna oriented along the z axis.

Figure 2.5 illustrates that each antenna has an equal phase shift from its adjacent element and each antenna element is fed separately. Controlling the signal phase and amplitude of closely spaced antenna elements, the emitted radio waves are combined to form a stronger wave in the predefined direction. Taking into account the equal space of d between elements, the time delay for the signal received by the second element (relative to the first element) can be calculated as

$$t_1 = \frac{d \sin \theta}{c}. \tag{2.1}$$

The parameter θ in (2.1) shows the angle between the y axis and the received signal, and c is the speed of light. On the basis of time delay, the phase shift
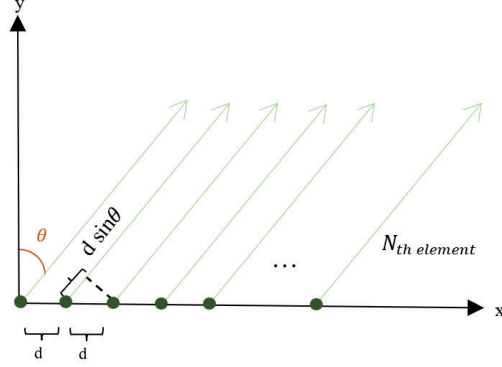
Figure 2.5: Uniform Linear Array

between the first two elements can be calculated as

$$\phi = e^{-j\omega_0 t_1}. \tag{2.2}$$

Assuming d as a half wavelength and $\omega_0 = 2\pi \frac{c}{\lambda}$ the phase shift can be calculated as

$$\phi = e^{-j2\pi \frac{d \sin \theta}{\lambda}} = e^{-j\pi \sin \theta}. \tag{2.3}$$

For the array consisting of N antenna elements, time delay, and the phase shift in the N_{th} antenna element relative to the first antenna element which is considered as a reference given in (2.4) and (2.5) respectively.

$$t_N = \frac{(N-1)\, d \sin \theta}{c} \tag{2.4}$$

$$\phi = e^{-j(N-1)\pi \sin \theta}. \tag{2.5}$$

Based on the equations above, the steering vector for the uniform linear array for N elements defined as a vector with length N of the array responses of the field from angle θ can be derived as

$$\alpha = \begin{bmatrix} e^{-j\pi \sin \theta} \\ e^{-j2\pi \sin \theta} \\ \dots \\ e^{-j(N-1)\pi \sin \theta} \end{bmatrix}. \tag{2.6}$$

2.4.2   Planar Array (PA)

Previously we highlighted the significance of array antennas in beamforming and now will focus on the specific type called uniform planar array (UPA). Figure 2.6 depicts the configuration of a UPA that achieves beamforming through phase shifters. Each square represents an antenna linked to a separate phase shifter

and the antennas are arranged like a matrix. This combination of antennas makes beam departure in two planes possible; however, the deployment of a large number of phase shifters makes the system complicated.
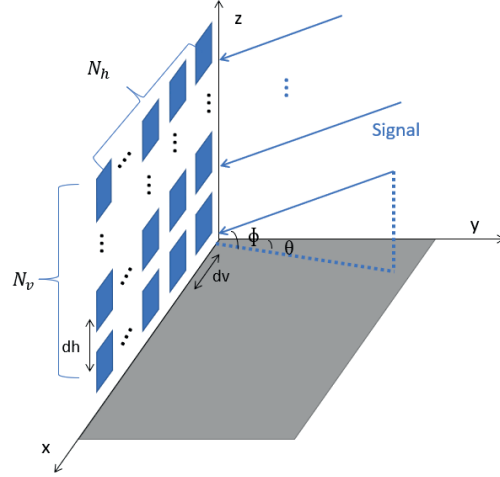
Figure 2.6: Uniform Planar Array

The total number of antennas is N_t and is equal to the product of N_v which is the number of antennas in the vertical direction and N_h which is the number of antennas in the horizontal direction. Each antenna element can be placed in (m, n) while m = 1,2,...,N_v and n = 1,2,...,N_h. The Angle of Arrival (AOA) and the Angle of Departure (AOD) have θ as azimuth and ϕ as elevation angles. The azimuth angle denotes the angle between the y axis and the direction of the signal in the xy plane, and the elevation angle is defined as the angle between the signal and the projection of the signal in the xy plane. AOD/AOA can be defined as (2.7) based on its two components [16] as

$$\Omega = [\theta, \phi]^T . \tag{2.7}$$

To derive the steering vector of the planar array, we consider a simple case of four elements. Antenna elements are separated by distance d from each other and have the coordination of x_p and y_p with values of 0 and d. The arrival signal has the azimuth angle of θ, which is the angle between the direction of the signal and the xy plane, and the elevation angle of ϕ, which is the angle between the signal and the x plane.

Taking the element at (0,0) as a reference element, the delay vector for other elements relative to the reference element is calculated using

$$t = \frac{1}{c} \left(x_p \cos\theta \cos\phi + y_p \sin\theta \cos\phi \right) . \tag{2.8}$$

Based on (2.2) and (2.8) and considering d as half-wavelength, the steering vector can be derived as

$$\begin{bmatrix} 1 \\ e^{-j\pi \sin\theta \cos\phi} \\ e^{-j\pi \cos\theta \cos\phi} \\ e^{-j\pi(\sin\theta \cos\phi + \cos\theta \cos\phi)} \end{bmatrix}. \tag{2.9}$$

Lab Test Setup

3.1   Overview of the MIMO verification system

The accuracy of MIMO functions can be evaluated using OTA measurement test methods, but these types of tests are usually difficult to implement and many details must be considered to obtain correct and reliable measurements. Therefore, it is important to develop test equipment that enables laboratory testing rather than OTA testing. For the lab measurements, the channel is modelled with the test equipment.

In Figure 3.1, the structure of the MIMO verification setup is shown, which works in mid-band with a centre frequency of 2.625 GHz. This system comprises three main components, Radio Unit (RU), antenna beam box, and DU. The RU consists of a total of 64 antennas, and it is worth noting that because this test system is reciprocity-based, the antennas in the RU can work as both receivers and transmitters depending on the UL or DL scenario of interest. The DU can be viewed as a BS. The BS consists of a baseband unit and a radio unit with a multiple antenna array. The baseband unit is controlled with a Moshell, which is a Linux shell adapted for the baseband, which together with the RU generates the signal to feed it into the beam simulation system, which is the Butler matrix in this lab setup. The antenna beam box, which consists of the two 32×16 Butler matrices, is the core of the test system. The beam box has 64 RF cables connected with RU and 32 RF ports towards the UE, corresponding to 16 directions for each of the two polarizations. The 16 outputs of the Butler matrix are connected to the Cellular Coaxial Network (CCN) before the UEs and act as an RF switch and define which of the UEs will receive the output. All test cases for the different combinations of UEs are conducted via the Citrix workspace, which connects the mentioned platforms remotely.

3.2   The Butler matrix

In the previous chapter, we extensively examined the uses and advantages of the Butler matrix. In this chapter, we will focus on the structure inside the antenna beam box. Specifically, the estimation procedure to acquire the antenna weights from the UL and the application to beamforming are examined.
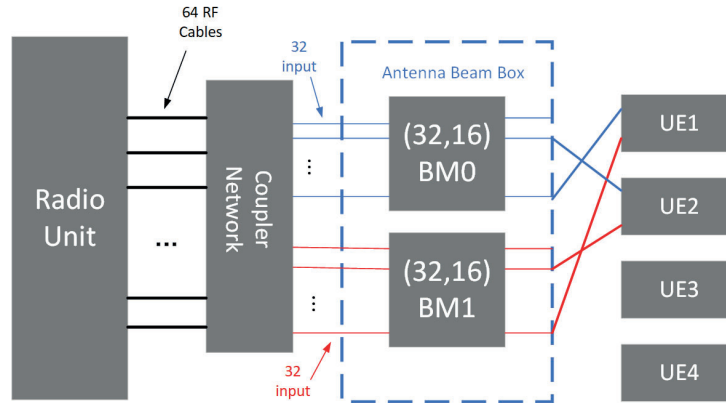
Figure 3.1: Lab setup

3.2.1 Hybrid coupler

Hybrid couplers with four ports can be seen as a small 2×2 Butler matrix in the system design. In the antenna beam box, two kinds of hybrid couplers are used to construct the system. 180° hybrid couplers and 90° couplers. A 180° hybrid coupler has two inputs and two outputs. When the signal is applied to the sum ports ($\sum$), two in-phase signals with the same amplitude will be generated from 1 and 2, and two 180° out-of-phase signals with the same amplitude will emerge when the signal is applied to the difference ports (Δ). On the contrary, two input signals are combined with 0° phase shifts in the sum ports, whereas in the difference ports, they are added with a phase difference of 180°. In Figure 3.2, a diagram of a 180° hybrid coupler is shown.

A 90° hybrid coupler, which is also known as a quadrature hybrid coupler, operates similarly; Two signals with a 90° phase difference and the same amplitude can be observed at the two outputs. Figure 3.3 shows a diagram of a 90° hybrid coupler.
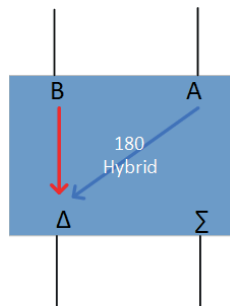
Figure 3.2: hybrid 180°
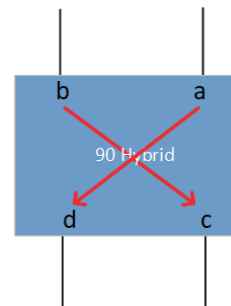
Figure 3.3: hybrid 90°

The phase states at the different ports of a 180° hybrid coupler can be repre-

sented by matrix using (3.1). The output of a 90° hybrid coupler can be calculated using (3.2).

$$\begin{bmatrix} \Sigma \\ \Delta \end{bmatrix} = \frac{1}{\sqrt{2}} \begin{bmatrix} 1 & 1 \\ j & -j \end{bmatrix} \begin{bmatrix} A \\ B \end{bmatrix} \tag{3.1}$$

$$\begin{bmatrix} c \\ d \end{bmatrix} = \frac{1}{\sqrt{2}} \begin{bmatrix} 1 & -j \\ -j & 1 \end{bmatrix} \begin{bmatrix} a \\ b \end{bmatrix}. \tag{3.2}$$

3.2.2 The 4×4 Butler matrix

Each 4×4 Butler matrix consists of three 180° hybrid couplers and one 90° hybrid coupler. The structure of a 4×4 Butler matrix is shown in Figure 3.4.
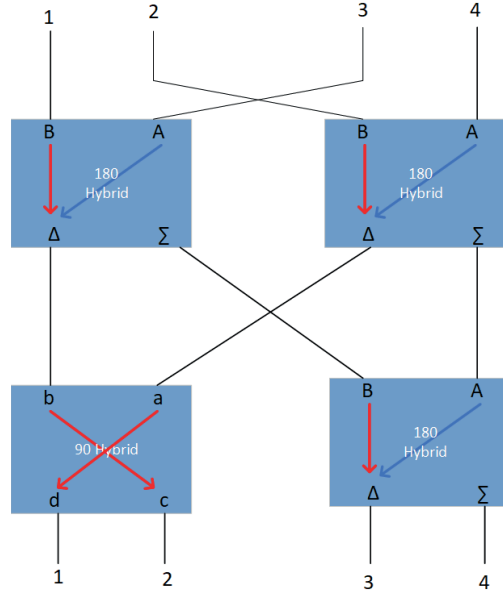
Figure 3.4: Structure of the 4×4 Butler matrix

Equation (3.3) shows the process for deriving the scattering matrix of the 4×4 Butler matrix. It should be noted that the first and third inputs exchange their sequences at the output by passing through the first layer and the third layer, and this process can be mathematically represented by multiplying with a scattering matrix $S1$ as

$$\begin{bmatrix} a \\ c \\ b \\ d \end{bmatrix} = \begin{bmatrix} 1 & 0 & 0 & 0 \\ 0 & 0 & 1 & 0 \\ 0 & 1 & 0 & 0 \\ 0 & 0 & 0 & 1 \end{bmatrix} \cdot \begin{bmatrix} a \\ b \\ c \\ d \end{bmatrix} = S1 \cdot X_{input1} = S3 \cdot X_{input3}, \tag{3.3}$$

where Sn represents the scattering matrix of the n_{th} layer of the Butler matrix. X_{inputn} represents the input signal of the nth layer. For the second layer of the

Butler matrix, the scattering matrix can be obtained using (3.1) and (3.2). The process is shown as

$$
\begin{bmatrix} \Delta_1 \\ \Sigma_1 \\ \Delta_2 \\ \Sigma_2 \end{bmatrix} = \begin{bmatrix} -j & j & 0 & 0 \\ 1 & 1 & 0 & 0 \\ 0 & 0 & -j & j \\ 0 & 0 & 1 & 1 \end{bmatrix} \cdot \begin{bmatrix} B_1 \\ A_1 \\ B_2 \\ A_2 \end{bmatrix} = S2 \cdot X_{input2}, \tag{3.4}
$$

where M_n represents the signal at port M in the nth hybrid coupler. The scattering matrix of the fourth layer of the Butler matrix can be derived similarly as

$$
\begin{bmatrix} d_3 \\ c_3 \\ \Delta_4 \\ \Sigma_4 \end{bmatrix} = \begin{bmatrix} 1 & -j & 0 & 0 \\ -j & 1 & 0 & 0 \\ 0 & 0 & -j & j \\ 0 & 0 & 1 & 1 \end{bmatrix} \cdot \begin{bmatrix} b_3 \\ a_3 \\ B_4 \\ A_4 \end{bmatrix} = S4 \cdot X_{input4}. \tag{3.5}
$$

The scattering matrix of the 4×4 Butler matrix can be derived by successive matrix multiplications of layers. The Butler matrix response $H_{4\times4}$ can be obtained from (3.6) as

$$
Y = H_d H_{4\times4} X = \frac{1}{2} \times H_d \cdot S4 \cdot S3 \cdot S2 \cdot S1 \cdot X
$$

$$
= \frac{1}{2} H_d \begin{bmatrix} 1 & -j & 0 & 0 \\ -j & 1 & 0 & 0 \\ 0 & 0 & -j & j \\ 0 & 0 & 1 & 1 \end{bmatrix} \cdot \begin{bmatrix} 1 & 0 & 0 & 0 \\ 0 & 0 & 1 & 0 \\ 0 & 1 & 0 & 0 \\ 0 & 0 & 0 & 1 \end{bmatrix} \cdot \begin{bmatrix} -j & j & 0 & 0 \\ 1 & 1 & 0 & 0 \\ 0 & 0 & -j & j \\ 0 & 0 & 1 & 1 \end{bmatrix} \cdot \begin{bmatrix} 1 & 0 & 0 & 0 \\ 0 & 0 & 1 & 0 \\ 0 & 1 & 0 & 0 \\ 0 & 0 & 0 & 1 \end{bmatrix} X
$$

$$
= \frac{1}{2} \begin{bmatrix} e^{j\theta} & 0 & 0 & 0 \\ 0 & e^{j\theta} & 0 & 0 \\ 0 & 0 & 1 & 0 \\ 0 & 0 & 0 & 1 \end{bmatrix} \begin{bmatrix} -j & -1 & j & 1 \\ -1 & -j & 1 & j \\ -j & j & -j & j \\ 1 & 1 & 1 & 1 \end{bmatrix} X
$$

$$
= \frac{1}{2} \begin{bmatrix} -j & -1 & j & 1 \\ -1 & -j & 1 & j \\ -j & j & -j & j \\ 1 & 1 & 1 & 1 \end{bmatrix} X. \tag{3.6}
$$

In (3.6), $Y = [y_i]$ is a column vector with each element y_i corresponding to the i_{th} network output (UE side). Similarly, $X = [x_i]$ is also a column where x_i is the input of the i_{th} network (antenna side) for DL. H_d is embedded in the system to compensate for the delay in the hardware group between two types of hybrid couplers in the system. Furthermore, θ is a frequency-dependent phase that varies according to the internal delay. In Matlab simulation, the phase is set to 0° from the beginning, so H_d is an identity matrix, and $Y = H_{4\times4}X$.

3.2.3   The 32×16 Butler matrix

As demonstrated in the preceding chapter, the scattering matrix of the 4×4 Butler matrix has been obtained. The 32×16 Butler matrix is constructed based on the
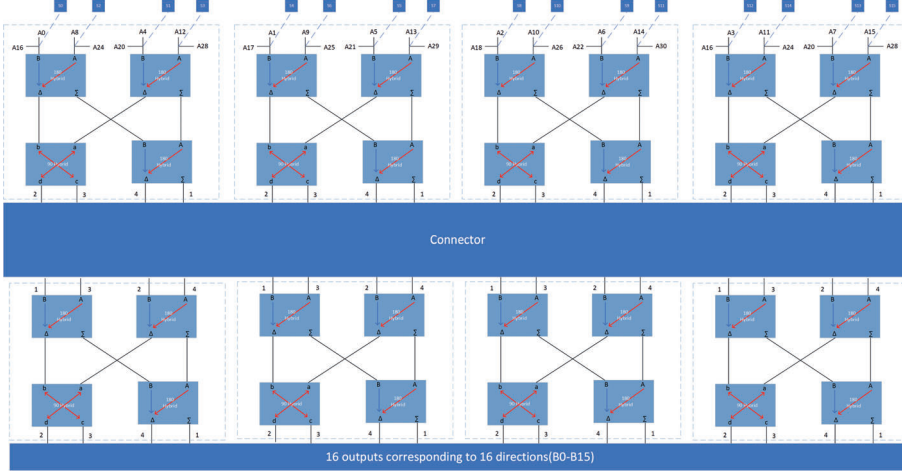
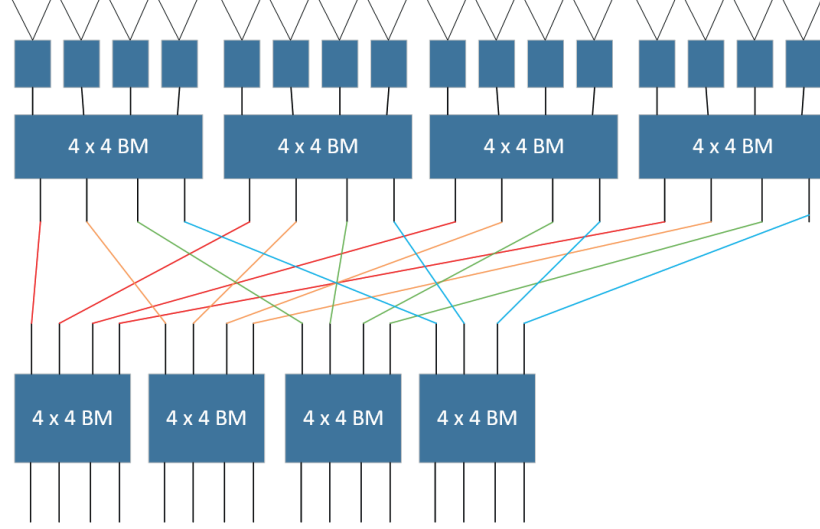**Figure 3.5:** Structure of the 32×16 Butler matrix

combination of the eight small Butler matrices and a 16 to 16 connector network. The structure of the system is shown in Figure 3.5.

The 16 outputs of the Butler matrix correspond to 16 directions of beamforming. In general, the system can add four different distinct phases to the input signal, i.e. 0°, 90°, 180°, and -90° corresponding to 1, j, -1, and -j in the scattering matrix. Additionally, the AAS comprises a 4×8 antenna array. To perform beamforming, the phase shift introduced to the subsequent antennas must be the same, thus the phase added on the last 4×4 antenna array should be identical to the preceding 4×4 array. So, the 32×16 Butler matrix can be viewed as a 16×16 Butler matrix where each input is split into two ports and applied on two antennas, i.e., the phase shift applied on the first antenna is the same as it on 17th. In the system design, 16 combiners are used to combine the same weights added on all two antennas into one input port of the Butler matrix in the DL. The details of the port-to-antenna mapping methods will be explained in the next chapter.

The scattering matrix of the 16×16 Butler matrix can be obtained in a similar way to that of the previous chapter. As shown in Figure 3.5, the first layer is constructed by the four 4×4 Butler matrix. The scattering matrix for the first layer can be derived using (3.10) as

$$S1 = I_4 \otimes H_{4\times4} = \begin{bmatrix} H_{4\times4} & (0)_{4\times4} & (0)_{4\times4} & (0)_{4\times4} \\ (0)_{4\times4} & H_{4\times4} & (0)_{4\times4} & (0)_{4\times4} \\ (0)_{4\times4} & (0)_{4\times4} & H_{4\times4} & (0)_{4\times4} \\ (0)_{4\times4} & (0)_{4\times4} & (0)_{4\times4} & H_{4\times4} \end{bmatrix}, \qquad (3.7)$$

where $\otimes$ is the Kronecker product, I_4 is a 4×4 identity matrix, $(0)_{4\times4}$ is a 4×4 matrix that has all its elements equal to zero. The structure of the connector network is shown in Figure 3.6. The scattering matrix of the connector layer can be derived as

Figure 3.6: Structure of the 32×16 Butler matrix

$$BM_{2,1_{input}} = \begin{bmatrix} 1000 & 0000 & 0000 & 0000 \\ 0000 & 1000 & 0000 & 0000 \\ 0000 & 0000 & 1000 & 0000 \\ 0000 & 0000 & 0000 & 1000 \end{bmatrix} \cdot \begin{bmatrix} BM_{1,1_{o}utput} \\ BM_{1,2_{o}utput} \\ BM_{1,3_{o}utput} \\ BM_{1,4_{o}utput} \end{bmatrix}, \tag{3.8}$$

where $BM_{a,b}$ represents a 4×1 matrix $\begin{bmatrix} BM_{a,b,1} & BM_{a,b,2} & BM_{a,b,3} & BM_{a,b,4} \end{bmatrix}^H$ that represents the four input or output ports of the b^{st} Butler matrix in a^{st} layer. Similarly, the other three Butler matrices in the second layer can be derived as

$$\begin{bmatrix} BM_{2,1,iutput} \\ BM_{2,2,iutput} \\ BM_{2,3,iutput} \\ BM_{2,4,iutput} \end{bmatrix} = \begin{bmatrix} I_4 \otimes \begin{bmatrix} 1 & 0 & 0 & 0 \end{bmatrix} \\ I_4 \otimes \begin{bmatrix} 0 & 1 & 0 & 0 \end{bmatrix} \\ I_4 \otimes \begin{bmatrix} 0 & 0 & 1 & 0 \end{bmatrix} \\ I_4 \otimes \begin{bmatrix} 0 & 0 & 0 & 1 \end{bmatrix} \end{bmatrix} \cdot \begin{bmatrix} BM_{1,1,output} \\ BM_{1,2,output} \\ BM_{1,3,output} \\ BM_{1,4,output} \end{bmatrix}$$

$$= S2 \cdot \begin{bmatrix} BM_{1,1_{o}utput} \\ BM_{1,2_{o}utput} \\ BM_{1,3_{o}utput} \\ BM_{1,4_{o}utput} \end{bmatrix}. \tag{3.9}$$

The scattering matrix of the third layer $S3$ is equal to $S1$. Similar to (3.6), the scattering matrix of the 16×16 Butler matrix can be expressed as (3.10) with the size of 16 columns and 32 rows. $Y = [y_i]$ is a column vector with 16 elements from y_0 to y_{15} corresponding to the i_{th} network output (UE side), $X = [X_i]$ is a column vector with elements from y_0 to y_{15} corresponding to the i_{th} network output (UE side). The scattering matrix of the 16×32 Butler matrix is given as (3.11).

$$Y = S3 \cdot S2 \cdot S1 \cdot X = H_{16 \times 16} X, \tag{3.10}$$

$$H_{16\times32} = \begin{bmatrix} H_{16\times16} \\ H_{16\times16} \end{bmatrix}. \tag{3.11}$$

It should be noted that all derivations presented for the Butler matrix are based on the assumption that the antenna knows its proper weight from the DU while implementing beamforming to a specific direction in the DL. As a result, only one out of the 16 outputs of the Butler matrix can show output power, indicating the power received by the UE in that direction, and other output ports will not receive any power due to the orthogonality of the phase shifts generated by the Butler matrix.

3.2.4   Uplink Butler matrix derivation

In the previous section, we obtained the Butler matrix for DL transmission. Our test platform employs one Butler matrix for both UL and DL, which provides a test scenario to check if the beamforming works effectively.

As the Butler matrix is bidirectional and follows channel reciprocity, if one UE is connected to a certain output of the Butler matrix, it can transmit the SRS through the Butler matrix to the BS and that can be received by each antenna with a certain angle of arrival given by the Butler matrix, the DL channel is the inverse of UL, we can assume that the phase shifts applied to antennas can be compensated by channel generated by the DL Butler matrix and gathered into a single output. In this section, we will focus on deriving the phase shift for each antenna in a way similar to the DL scenario. According to (3.2) and (3.1), when the hybrid coupler is used in a reverse way, Δ and Σ ports are viewed as input ports, and A and B ports are viewed as output ports, thus the UL transfer function for a 4×4 Butler matrix is shown as

$$
\begin{aligned}
H_{4\times4uplink} &= \frac{1}{2} \cdot \begin{bmatrix} e^{j0} & e^{-j\frac{\pi}{2}} & e^{j0} & e^{j0} \\ e^{-j\frac{\pi}{2}} & e^{j0} & e^{-j\pi} & e^{j0} \\ e^{-j\pi} & e^{-j\frac{3\pi}{2}} & e^{-j0} & e^{-j0} \\ e^{-j\frac{3\pi}{2}} & e^{-j\pi} & e^{-j\pi} & e^{-j0} \end{bmatrix} \\
&= \frac{1}{2} \begin{bmatrix} 1 & -j & 1 & 1 \\ -j & 1 & -1 & 1 \\ -1 & j & 1 & 1 \\ j & -1 & -1 & 1 \end{bmatrix}.
\end{aligned}
\tag{3.12}
$$

The first layer for the UL is the third layer of the DL but with different input ports. The scattering matrix for the first layer and the third layer for the UL is the same, shown in (3.13). The second layer is the same as $S2$ in the DL, as shown in (3.14).

$$
\begin{aligned}
S1_{up} &= S3_{up} = I_4 \otimes H_{4\times4uplink} \\
&= \begin{bmatrix} H_{4\times4uplink} & (0)_{4\times4} & (0)_{4\times4} & (0)_{4\times4} \\ (0)_{4\times4} & H_{4\times4uplink} & (0)_{4\times4} & (0)_{4\times4} \\ (0)_{4\times4} & (0)_{4\times4} & H_{4\times4uplink} & (0)_{4\times4} \\ (0)_{4\times4} & (0)_{4\times4} & (0)_{4\times4} & H_{4\times4uplink} \end{bmatrix}
\end{aligned}
\tag{3.13}
$$

$$S2_{up} = S2 = \begin{bmatrix} I_4 \otimes \begin{bmatrix} 1 & 0 & 0 & 0 \end{bmatrix} \\ I_4 \otimes \begin{bmatrix} 0 & 1 & 0 & 0 \end{bmatrix} \\ I_4 \otimes \begin{bmatrix} 0 & 0 & 1 & 0 \end{bmatrix} \\ I_4 \otimes \begin{bmatrix} 0 & 0 & 0 & 1 \end{bmatrix} \end{bmatrix} \tag{3.14}$$

The scattering matrix of the Butler matrix for the UL can be obtained using

$$\begin{aligned} H_{16 \times 16up} &= S3_{up} \cdot S2_{up} \cdot S1_{up} \\ H_{32 \times 16up} &= [H_{16 \times 16up}, H_{16 \times 16up}] . \end{aligned} \tag{3.15}$$

3.2.5 Multi-user test based on the Butler matrix

In Section 3.1, it is established that the passive beamforming implemented by the Butler matrix gives fixed directions because of the fixed phase shifts generated by the Butler matrix. Therefore, the weight applied to the antenna supports the beams limited to the 16 directions, later shown in the Table 4.2.

In practical scenarios, while testing MU-MIMO, precoding is often used to achieve channel orthogonality and eliminate interference among different UEs. However, in our lab test system, the phase shifts given by the Butler matrix for each UE are orthogonal to those of the other 15 UEs as shown in (3.16). This implies that when the UE is connected with one of the 16 directions to simulate the DL scenario, the remaining fifteen outputs of the Butler matrix should not receive any power from the outputs of the Butler matrix.

$$\begin{aligned} W_i \cdot H_n &= 0 \\ subject\ to \quad i, n &= 0, 1, 2, ...15\ and\ i \neq n, \end{aligned} \tag{3.16}$$

where $W_i = [w_{i0}, w_{i1}, w_{i2}...w_{i31}]$ is a vector with 32 columns indicating the weights applied on the 32 antennas for the ith UE. $H_n = [h_{n0}, h_{n1}, h_{n2}...h_{n31}]^H$ is a column vector with 32 elements representing the phase-shift matrix generated for the nth port by the Butler matrix in the DL.

Based on the characteristics mentioned above, and taking into account that the matrix obeys the property while supporting multiple UEs in the DL, the weight matrix for each UE can be added directly. Consequently, a unified weight matrix with the size 1×32 can be obtained for scenarios that support multiple UEs. As a result, only specific ports that are connected to the UEs should receive power.

3.3 Advanced Antenna System (AAS)

3.3.1 The AAS structure

The AAS used in this project consists of many antenna sub-arrays that are organized with relative phase shifts and gains [7]. There are typically 16 or 32 subarrays in the AAS models. There could be two to four cross-polarized antennas in the

subarray. Each subarray is connected to two RF chains, one per polarization. The subarray works as one cross-polarized antenna; however, its larger area provides higher gain. Figure 3.7 shows a typical antenna array with subarrays of dual-polarized antennas. A dual-polarized array will increase the capacity of the system by responding to horizontally and vertically polarized radio waves simultaneously. In Figure 3.7 a typical test image is shown. Typically, ±45 degree dual-polarized antennas are used in the AAS.

Figure 3.7: Typical subarray

In conventional antenna systems, the RF chain and the passive antennas are physically separated. However, the increased number of antennas in modern arrays will cause more complexity and interference in the radio system feeder if separate RF cables are used to connect them [17]. The most important part of the AAS is an active transmitter and receiver RF chain that intelligently integrates with a passive antenna array into one hardware unit. In addition to remarkably reducing the size of the AAS, this integration increases throughput, while reducing power consumption and cable loss.

Figure 3.8 shows how the subarrays are fed with their own RF chain. Generally, AAS is the main targer of the laboratory test in order to prepare it for real applications and field tests. In our project, we apply performance evaluation to the beamforming system used in laboratory.

3.3.2 Functionality of the AAS

The rectangular antenna array, where beamforming is used to direct high-gain beams at various angles, serves as the foundation for the operation of the AAS. A constructive combination of the individual antenna elements will form the main lobe to transmit the energy in the intended direction, illustrating that radio signals will be precoded with phase and amplitude shifts before being applied to each element for transmission. The total gain of the system will be determined by the number of available elements.

3.4 Device-specific pattern

In TDD operation, the same carrier frequency is used, and UL and DL transmissions are separated per cell. Therefore, the UL and DL transmissions do not overlap in time. Two types of dynamic and static UL-DL allocations are available in the TDD operation. Selecting static UL-DL allocation is favorable, as it

Figure 3.8: AAS structure with the different subarrays

helps prevent troublesome interference situations. To implement static allocation, a fixed scheduling pattern can be applied in each BS.

An important element in TDD systems is the ability to establish a long guard period in which there is no UL or DL transmission. This period is essential to switch from the UL to the DL and vice versa. The switching time is when the DL ends and before the start of the UL. This time must support the time required for the electronic circuits both in the BS and in the UE to switch from the DL to the UL. Figure 3.9 shows a typical UL-DL pattern in a TDD system [15].

Figure 3.9: Device specific UL-DL pattern

As discussed in the previous chapter, the SRS is used for UL channel sounding and can be considered equivalent to the CSI-RS in the DL while they both are means for channel sounding. In our test case, the period of one frame is 10 ms, and each slot is 0.5 ms. The SRS data is measured and collected during the UL slot. Channel estimation is scheduled for three DL transmissions, switching, and one UL transmission. The Sub-Carrier Group (SCG) refers to particular parameters

and settings indicating how the UE sends the SRS. It shows the number of the Physical Resource Blocks (PRBs) in the bandwidth, each SCG corresponding to two PRBs. In our measurement, we employed 273 PRBs in the whole bandwidth. In this project, we measure the 68th SCG which corresponds to the 136th and 137th PRBs, located in the center frequency.

3.5 Insertion loss calculations

The system has a fixed insertion loss, which can help us to judge if we receive the expected power per each UE. The expected insertion loss is shown in Table 3.1. Note that the insertion loss is for the Single-User (SU) case. For SU, we expect to receive around -39.02 dBm of power in the measurement. When the number of UEs is doubled, the power received by each UE will be split in half, and in the dB domain each UE will have a 3dB loss.

Table 3.1: Insertion loss calculations table

Insertion loss	Power(dB)	PDSCH power received (dBm)
Output power of RU	17.02	17.02
RF cable1	0.53	16.49
32×16 BM + attenuator	25	-8.51
Fixed attenuator	30	-38.51
RF cable2	0.531	-39.042
PDSCH power on UE		-39.042

Simulation

4.1 AAS construction

From Section 3.3 we know that the AAS has 32 subarrays in the shape of a 4×8 configuration. Each subarray contains four cross-polarized dipole antennas in the shape of 4×1 antenna elements. For the simulations, we can use Matlab to construct each subarray and then shape the array to an AAS shape. It should be noted that the antennas in each antenna array share the same weights. The distance between each subarray vertically is 2.03λ, and horizontally 0.513λ. The AAS system in the Matlab simulations is shown in Figure 4.1. The four vertical dots with the same color antennas represent four antennas in one subarray.

Array Geometry

Array Span:
X axis = 0.000 mm
Y axis = 308.610 mm
Z axis = 661.307 mm
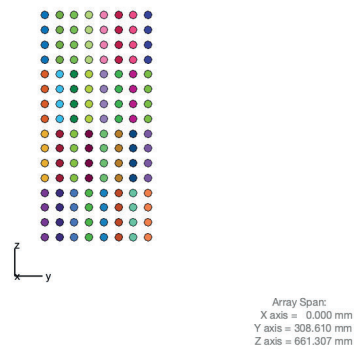
Figure 4.1: AAS structure in the simulation

4.2   The Butler matrix simulation

The test system can test a maximum of eight outputs, namely $B1$, $B2$, $B4$, $B5$, $B6$, $B9$, $B10$, and $B13$ due to the limitations of the CCN. These outputs correspond to specific directions, representing left, upleft, down, boresight, up, right, upright, and very right/left. The phase change generated by the Butler matrix for the UL is given in Table 4.1, where (r, c) shows the coordinates of the antenna located in the rth row and the cth column. The planar array under test has four rows and eight columns. We only show columns from zero to three, including 16 antennas; the other four columns (columns four-seven) are a copy of columns zero to three, and as a result, we can obtain the phase shift of 32 antennas in the AAS using the Butler matrix in the UL direction. The table contains complex numbers that represent phase shifts added to the antennas. Complex 1 means a phase shift of 0 degrees. Similarly, complex $-j$ represents 270 degrees, complex -1 represents 180 degrees, and complex j represents 90 degrees.

Table 4.1: Phase shifts for the uplink Butler matrix

(r,c)/Output	B1	B2	B4	B5	B6	B9	B10	B13
(0,0)	1	$-j$	1	1	$-j$	$-j$	-1	1
(0,1)	$-j$	-1	1	1	j	1	$-j$	-1
(0,2)	-1	j	1	1	j	j	1	1
(0,3)	j	1	1	1	j	-1	j	-1
(1,0)	1	1	$-j$	1	1	$-j$	$-j$	1
(1,1)	$-j$	$-j$	$-j$	1	1	1	1	-1
(1,2)	-1	-1	$-j$	1	1	j	j	1
(1,3)	j	j	$-j$	1	1	-1	-1	-1
(2,0)	1	j	-1	1	j	$-j$	1	1
(2,1)	$-j$	1	-1	1	j	1	j	-1
(2,2)	-1	$-j$	-1	1	j	j	-1	1
(2,3)	j	-1	-1	1	j	-1	$-j$	-1
(3,0)	1	-1	j	1	-1	$-j$	j	1
(3,1)	$-j$	j	j	1	-1	1	-1	-1
(3,2)	-1	1	j	1	-1	j	$-j$	1
(3,3)	j	$-j$	j	1	-1	-1	1	-1

4.3   Beam separation for horizontal and vertical directions

Beamforming can be seen as a linear precoding method based on the Singular Value Decomposition (SVD) of the channel, which can be performed with ideal CSI. In this case, the channel is decomposed into a complex unitary matrix U multiplied by a rectangular diagonal matrix (Σ) and further multiplied by the

conjugate transpose of another complex unitary matrix (V^*) as

$$H = U\Sigma V^*. \tag{4.1}$$

We take the first singular vector of U to perform beamforming. Taking our test scenario as an example, the AAS has 32 RF chains for one polarization per layer, and the channel generated by the Butler matrix can be decomposed into a continuous product of three matrices shown in (4.1).

In this master thesis, a cable network in the Butler matrix is used to establish connections among all antennas. Next, we plot the beam shapes for multiple UEs with the help of Matlab. The weight matrix for a system comprising 32 antennas can be acquired from the UL beamforming table, and the final weight matrix for four UEs can be obtained by summing up the weight matrix for each UE. According to the AAS system described above, each subarray consists of four cross-polarized antenna elements, but works as one antenna port. The relationship between the outputs of the Butler matrix and the directions of the beamforming is shown in Table 4.2.

Table 4.2: The Butler matrix outputs and physical beamforming angle

B3	B7	B11	B15
B2	B6	B10	B14
B1	B5	B9	B13
B0	B4	B8	B12

According to (2.1), a 90°phase shift in the horizontal direction between two adjacent antennas results in a delay distance of $\frac{90}{360}\lambda = \frac{1}{4}\lambda$, which leads to a separation of $\arcsin\frac{1/4\lambda}{0.513\lambda} = 29.16°$ between adjacent beams horizontally. Similarly, we can obtain the vertical separation of two beams which is equal to $\arcsin\frac{1/4\lambda}{2.05\lambda} = 7.07°$. Using a similar approach, the 180°phase difference of two adjacent antennas will result in a 77.07°angle horizontally and a 14.25°angle difference vertically. The beam separation in horizontal directions is shown in Figure 4.2(a), and the beam separation in vertical directions is shown in Figure 4.2(b).
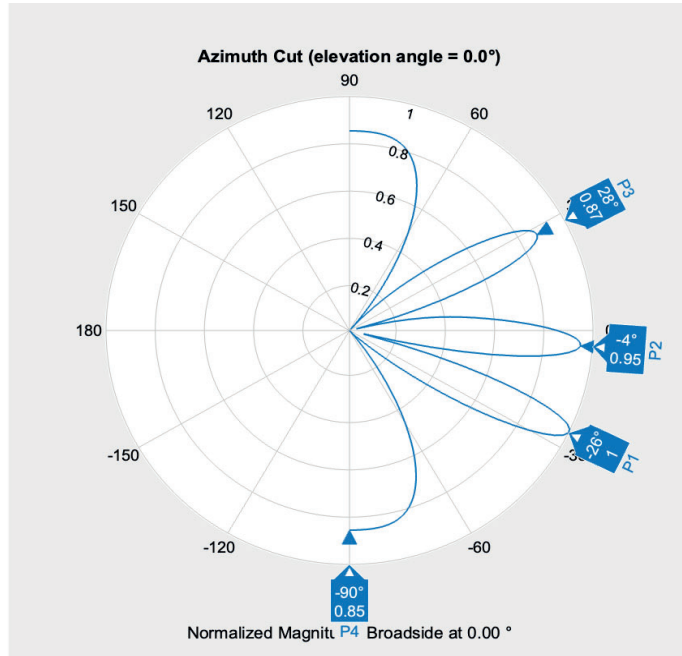
(a) Beam pattern (polar plot) in the horizontal direction
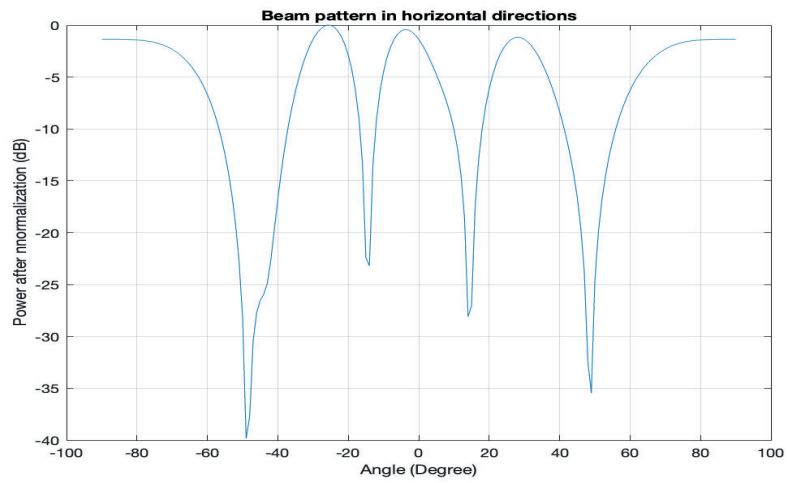
(b) Beam pattern in the horizontal direction

Figure 4.2: Beam separation in the horizontal direction
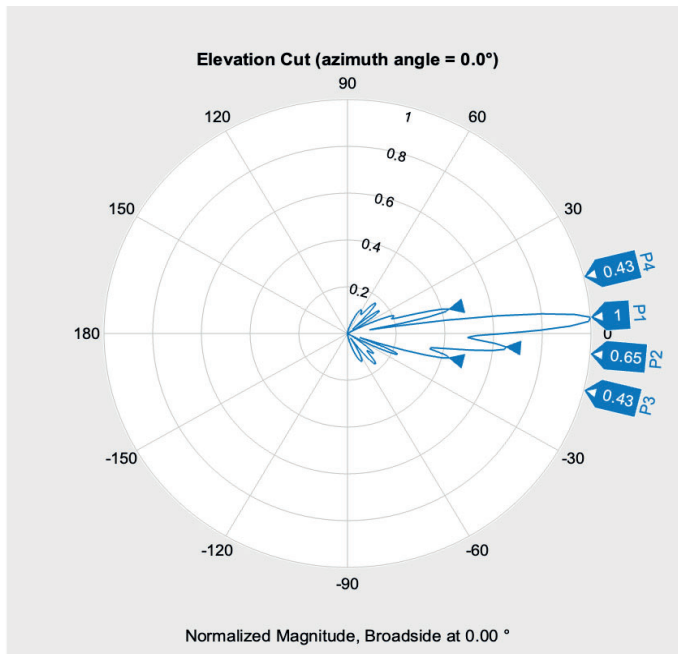
(a) Beam pattern (polar plot) in the vertical direction
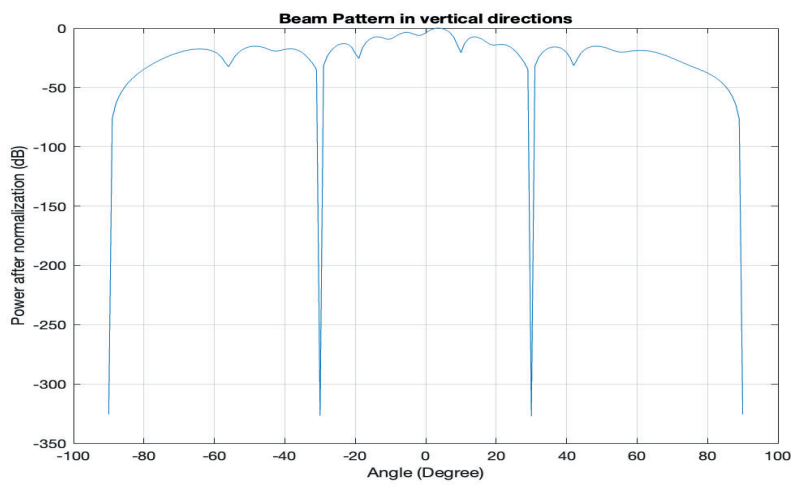
(b) Beam pattern in the vertical direction

Figure 4.3: Beam separation in the vertical direction

Measurements

5.1 DL measurement

To validate the simulation results from the previous chapter, it is necessary to perform measurements in real lab scenarios. Comparisons between simulations and measurements make it possible to evaluate the performance of the system under real conditions. In scenarios with one UE, the BS will be able to generate a beam with optimized quality and strength. However, in multi-user scenarios, interference mitigation and beam isolation will be significant issues. To ensure that each UE is provided with a reliable and efficient connection, it is necessary to properly separate the beams. Interference cancellation techniques and adaptive signal processing algorithms are usually used for this purpose. Power interference refers to unwanted interference from other UE beams, which can negatively affect the system's performance. Using PDSCH measurements, it is possible to quantify the level of power interference and analyze its impact on the data rate and signal quality. These measurements provide a valuable perspective on the beam separation technique.

The subsequent section presents PDSCH measurements for SU-MIMO and MU-MIMO scenarios. Each UE supports two layers, and measurements are performed for two UEs with four layers and four UEs with eight layers. In our lab setup, eight outputs of the Butler matrix are selected out of 16 outputs. The CCN acts as an RF switch between the Butler matrices, and the UEs can be deployed remotely through the Citrix workspace by selecting the outputs. To make the testing process easier, it is helpful to view the layout in the CCN corresponding to the beam directions. As an example, Figure 5.1 depicts the selected outputs of the Butler matrix in circle shapes. To simulate the UEs at different locations, we used the UE simulator and spectrum analyzer.

Viavi is connected to different radio cards and is responsible for providing the power to UEs. For conducting all the measurements, the spectrum analyzer in Figure 5.2 is used as an interface. The information related to the power per reference signal is shown in the frame summary. A screenshot of the VIAVI UE simulator is given in Figure 5.3.

33
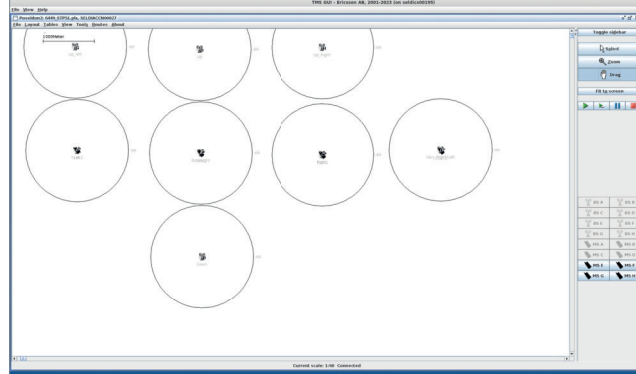
Figure 5.1: CCN with 8 directions of the UEs
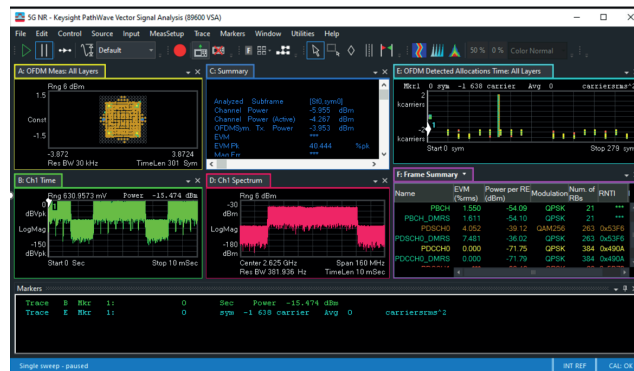
Figure 5.2: Spectrum analyzer for PDSCH power measurements

Table 5.1 presents the PDSCH measurements for the $B1$, $B5$, $B6$, and $B13$ directions individually and illustrates the throughput and power received by each UE, as well as EVM values when the BS transmits in two layers.

Table 5.1: PDSCH power measurements for 1 UE

Locations	Throughput	EVM (%rms)	PDSCH (dBm)
boresight	737	4.052	-39.12
left	737	7.732	-38.82
very right	737	3.882	-38.87
up	737	3.794	-38.73

The EVM is also known as the relative constellation error (RCE), and it is the magnitude of the vector in the IQ plane, which is between the ideal constellation diagram points and the points that are received from the receiver side (the
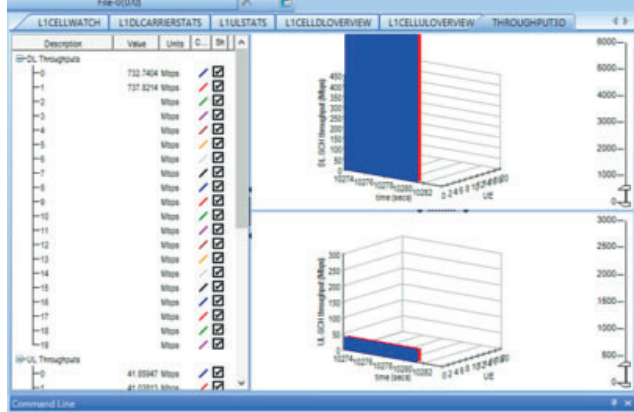
Figure 5.3: VIAVI UE simulator

constellation diagram of the received signal). Tables 5.2 to 5.4 show different combinations of the outputs of the Butler matrix. Table 5.2 shows the measurements for two UEs.

Table 5.2: PDSCH power measurements for 2 UEs

Location	Throughput	EVM (%rms)	PDSCH (dBm)
very right	737	5.912	-42.32
up	727	7.327	-42.20

Location	Throughput	EVM (%rms)	PDSCH (dBm)
boresight	727	6.389	-42.55
up	737	4.298	-42.07

Location	Throughput	EVM (%rms)	PDSCH (dBm)
right	737	6.788	-42.36
very right	737	7.461	-48.35

Location	Throughput	EVM (%rms)	PDSCH (dBm)
upleft	737	4.624	-41.85
right	737	4.418	-41.97

It is clear from Table 5.4 that although $B5$, which corresponds to the boresight, receives enough PDSCH power, the throughput value is lower than the expected amount and the EVM is also higher than in other directions. To make it clear and

Table 5.3: PDSCH power measurements for B1, B5,
B6, B9

Location	Throughput	EVM (%rms)	PDSCH (dBm)
left	730	6.240	-45.23
boresight	737	28.42	-45.58
right	737	15.4	-45.32
up	737	6.255	-45.20

Table 5.4: PDSCH power measurements for B1, B4,
B5, B9

Location	Throughput	EVM (%rms)	PDSCH (dBm)
left	737	5.096	-45.26
boresight	550	37.21	-45.61
right	737	4.508	-45.26
down	551.8	6.512	-52.32

to search for the reasons behind it, we will study the measured SRS trace in the
following section.

In addition to all the combinations that provide the expected throughput and
power, during the measurement process, we noticed that the combinations with a
down direction, called $B4$, receive lower power and small throughput values.

The table above highlights an issue in the down direction and in the following
sections, the root causes for this issue are investigated and studied in detail.

5.2   UL measurement

The previous chapter describes how the Butler matrix is used to simulate AOA
in a real channel. On the basis of reciprocity, the weights added to the antenna
from the Butler matrix used to perform beamforming in the DL are estimated by
the SRS. Note that it is impossible to measure phase shifts on antennas in the DL
once transmission starts because of high throughput; however, according to the
reciprocity assumption, the phase shifts can be estimated from the UL. Therefore,
it is a more direct way to measure the phase shift in the UL rather than observing
the power in the DL.

5.2.1   Testing method

The phase shifts applied to the 32 antennas when transmitting the data stream in
real scenarios cannot be measured due to equipment limitations. The first place
where we can measure the signals for the UL is in the DU. The place where we
record the data stream is shown in Figure 5.4. To process the different measure-
ments in a parallel way in the CPU, a Fast Fourier Transform (FFT) is embedded

in the RU to transfer the signal from the antenna space into the beam space. Instead of obtaining 32 phase shifts each time, we will receive one peak within 32 beam locations in the beam space showing the direction of the beam.
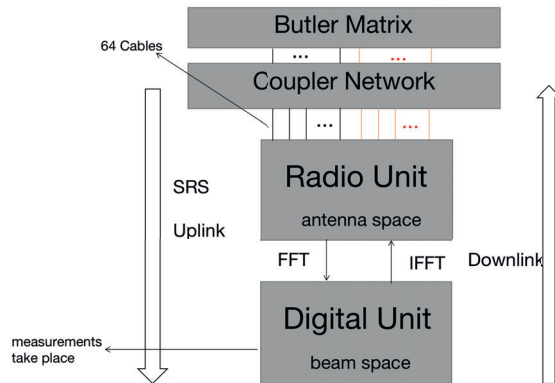
Figure 5.4: System for the measurements

5.2.2   Obtaining the SRS traces

The measurements are done by running a script after putting the UE in different directions for testing in the CCN. During transmission, the SRS is transmitted with specific parameters. From the received parameters, we can conclude that each SRS consists of eight lines that include several parameters, such as the ID of the cell, the ID of the UE, the name of the trace, the weights for the eight antennas, and the receiver layer. We only pick the ID for the UEs, the layer number, the polarization, and the weights, and export the CSV file.

To find the reason for the imperfect measurements shown in Table 5.4, we ran test cases for $B1$, $B4$, $B5$, and $B9$ three times and saved the scripts. To make the comparison with the measurement for the combination shown in Table 5.3, we also tested the cases for $B1$, $B5$, $B6$, and $B9$.

Result Analysis

6.1 Beam space and antenna space

As mentioned in Chapter 4, the SRS is measured in the UL for channel sounding purposes, the data is in the beam space and need to be transferred to the antenna space. The antenna space considers each antenna element and its radiation pattern individually within the array, without considering the beamforming characteristics. However, for this transmission, the ports are not assigned directly to the physical antennas [15]. In this process, a mapping function is used to map the M SRS ports to the N physical antennas. For high-frequency connections, NR devices usually use several antenna panels directed in different directions. Mapping the SRS to these antenna panels is equivalent to mapping the SRS ports to the physical antenna ports. Transmission from the aforementioned antenna panels will be associated with the separate mapping. The mapping functions are integrated within the whole system and Figure 6.1 shows the steps to the SRS transformation.
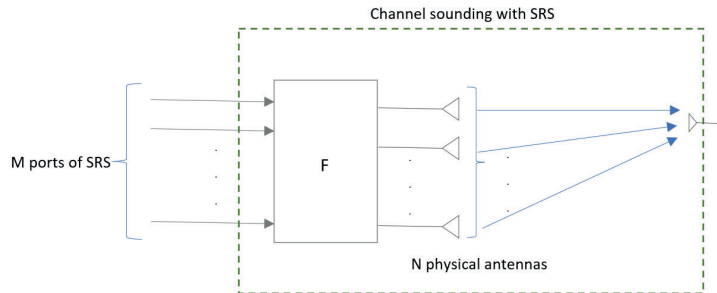
Figure 6.1: Mapping function to map the SRS ports to the physical antennas

The reception of SRS traces in the UL in the beam space facilitates the comparison between the measurement and the theoretical values. Figures 6.2(a) and 6.2(b) illustrate the validity of the measurements compared to the simulated data. The graphs show the location of the beam in the beam space for the $B9$ direction corresponding to the right in the output of the Butler matrix.
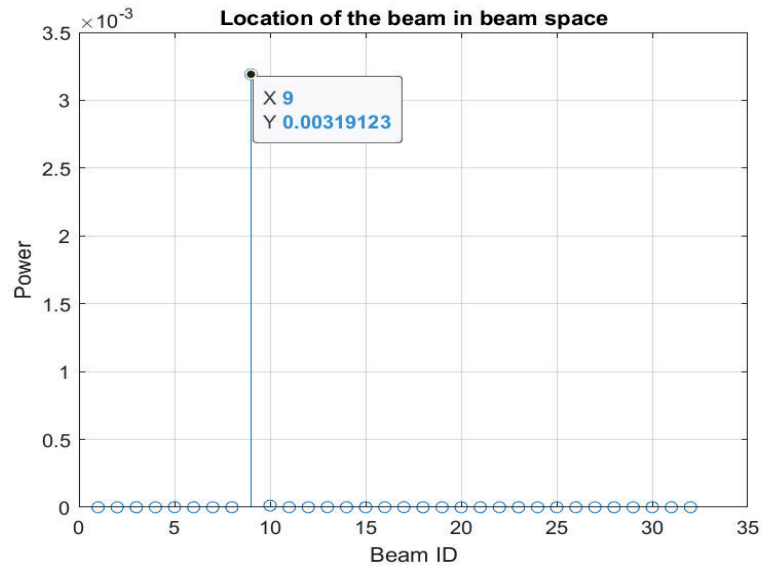
(a) Beam location from measurement
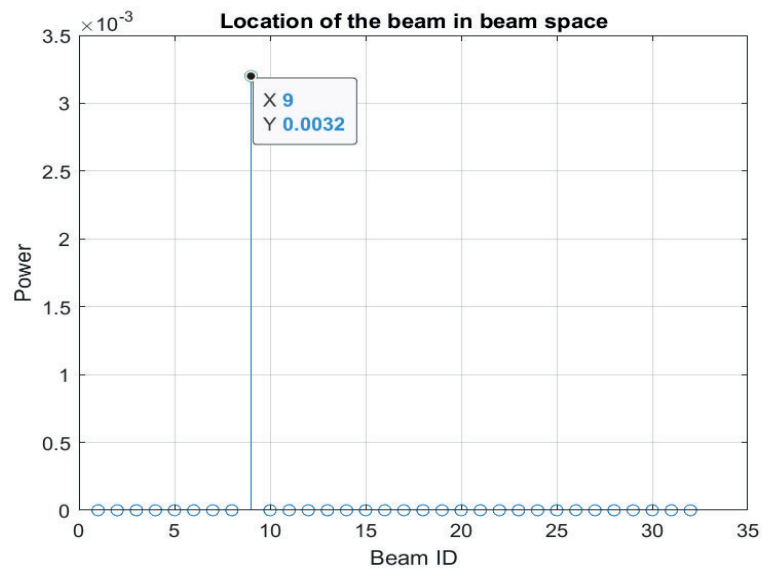
(b) Beam location from simulation

Figure 6.2: Location of the beam in the beam space

In Figure 6.2(b), the values at the other beams are zero, which means that there is no power leakage at the other locations. However, in real measurement scenarios, there are leakages to locations other than the main beam location; Figure 6.3 shows a slight power leakage as an example. For a better illustration, we set the power of the main beam to zero.
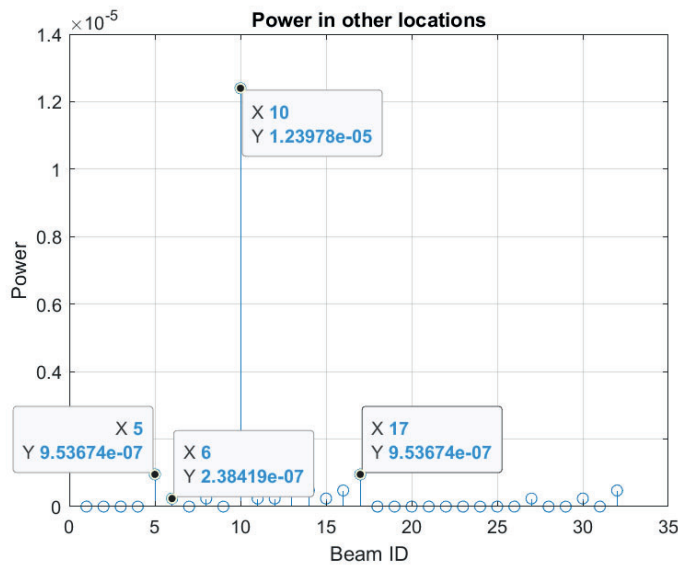
Figure 6.3: Power in other locations other than the main beam

6.2   Phase shift analysis

In the previous chapter, we have explained that the Butler matrix consists of phase shifters; therefore, it is one of the key tasks in our thesis to investigate the temporal variation of phases applied to antennas. From the scatter plot, we can derive the angle of each data point and wrap the angle within the range of 0 to 360 degrees. It is essential to note that this angle contains the original phase shift added on the first antenna. From the simulation of the Butler matrix, we also know the phase values in the Butler matrix table, which shows the phase difference between the antenna tested and the first antenna. Consequently, it is necessary to subtract the original phase shifts from the 2nd to the 32nd antenna to obtain phase differences in each slot.

6.3   Beam direction mapping

The determination of the beam direction can be done through measurements in the beam space from the SRS traces. The estimated direction allows us to assess the deviations from the expected directions and, consequently, evaluate the impact of phase errors on the beamforming directions. The process is shown in the following subsections and it consists of oversampling and FFT, curve fitting, and direction mapping.

6.3.1   Oversampling and FFT

As established in Section 6.1, each peak in the beam space corresponds to one beam direction. In Section 6.2, we transformed the beam space into the antenna space to obtain the phase shifts applied on the antennas using IFFT. Hence, it is necessary to use FFT to transform the antenna space back to the beam space. It should be noted that this transformation is done in two dimensions, since we reshape the 32 beam locations into a 4*8 matrix to match the antenna shape. To increase the accuracy of the beam direction estimation, we performed interpolation with an oversampling factor of 16. Hence, we obtain a matrix with the size of 64*128 shown in Figure 6.4. Here, we pick only one layer as an example.
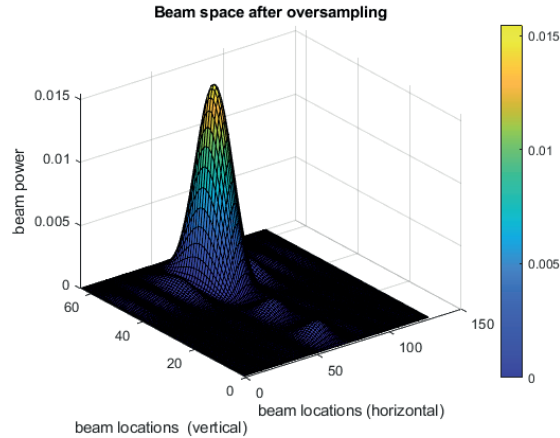
Figure 6.4: Beam space after oversampling

6.3.2   Curve fitting

Curve fitting is a widely employed technique for processing discrete data in the scientific field [18]. The power leaks shown in Section 6.1 will cause a shift in the peak after oversampling in beam space. To calculate the deviation between the peak position in the simulation results and the peak position in the measurement results, we need to obtain a continuous function instead of a discrete data point. In this thesis, we employ two methods, polynomial regression and Taylor expansion.

Polynomial regression

Polynomial fitting can be used for a linear problem, commonly addressed using the least squares (LS) method [19], aiming to minimize the sum of the squares of vertical errors between the data points (x_1, y_1), (x_2, y_2) ...(x_m, y_m) and the corresponding polynomial curve. The expression is given in as

$$p(x) = p_1 x^n + p_2 x^{n-1} + ... + p_n x + p_{n+1}, \tag{6.1}$$

where p_n is the coefficient for the nth degree polynomial that is the best fit for the data points. In this thesis, we choose $n = 2$, using quadratic fitting to simplify the process. Initially, we search for the peak location within a 64*128 matrix after oversampling shown in Figure 6.4 and set the coordinate as (0,0). Then we select four additional data points surrounding the peak in both dimensions to facilitate the fitting process, as shown in Figure 6.5. The fitting is done in both dimensions. In this section, we focus on five data points ($D0$, $D1$, $D1$, $D2$, $D3$, $D4$) in one dimension to explain the procedure.

Figure 6.5: Data selection for fitting

After fitting the curve with the data points, the graph is shown in Figure 6.6. As expected, the real peak of the continuous function is located between the two oversampled data points. It is shown in the Figure that the peak is located within the interval between two sample points, we denote the deviation from $D0$ to the real peak as Δx. The quadratic fitting formula including derivation is shown as

$$p(x + \Delta x) = p_1 (x + \Delta x)^2 + p_2 (x + \Delta x) + (x + \Delta x). \tag{6.2}$$

In the previous paragraph, we set the origin x = 0, so $p(0)$ corresponds to the maximum sampled value. The estimated peak value is

$$p(\Delta x) = p_1 (\Delta x)^2 + p_2 (\Delta x) + \Delta x. \tag{6.3}$$

At the peak, first-order derivatives have zero value. This implies that

$$p'(\Delta x) = 2p_1 \Delta x + p_2 + 0 = 0, \tag{6.4}$$

and the deviation for one dimension Δx can be calculated as

$$\Delta x = -\frac{p_2}{2p_1}. \tag{6.5}$$
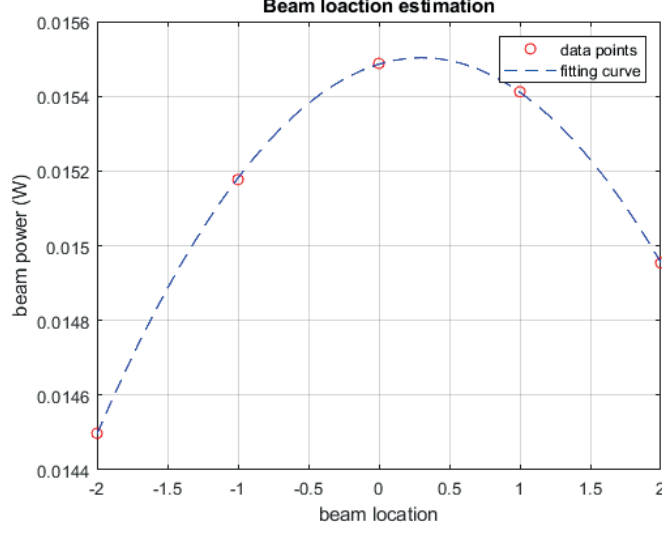
Figure 6.6: Data points and fitting curve

Since the deviation occurs in both dimensions, the process from (6.3) to (6.5) needs to be repeated once more to obtain the deviation in vertical dimension Δy. The final coordinate of a peak is $(0+\Delta x, 0+\Delta y)$.

Taylor expansion

Similarly, we started by finding the peak in the beam space and selected data points surrounding the peak, the peak in the middle is set as $D5$ with coordinate $(0,0)$. Taylor series approximation to the first order for one dimension is in (6.6) according to [20],

$$
\begin{aligned}
f(x + \Delta x, y) &\approx f(x, y) + \Delta x f_x(x, y) \\
f(x, y + \Delta x) &\approx f(x, y) + \Delta y f_y(x, y).
\end{aligned}
\tag{6.6}
$$

Then we can obtain the partial derivative for one dimension as

$$
\begin{aligned}
f_x(x + \Delta x, y) &\approx f_x(x, y) + \Delta x f_{xx}(x, y) \\
f_y(x, y + \Delta x) &\approx f_y(x, y) + \Delta y f_{yy}(x, y).
\end{aligned}
\tag{6.7}
$$

Based on Taylor expansion in two dimensions in (6.8), according to [20]

$$
f(x + \Delta x, y + \Delta x) \approx f(x, y) + \Delta x f_x(x, y) + \Delta y f_y(x, y) + \Delta x \Delta y f_{xy}(x, y). \tag{6.8}
$$

We can obtain the partial derivative for the two dimensions as

$$
\begin{aligned}
f_x(x + \Delta x, y + \Delta x) &\approx f_x(x, y) + \Delta x f_{xx}(x, y) + \Delta y f_{xy}(x, y) + \Delta x \Delta y f_{xxy}(x, y) \\
f_y(x + \Delta x, y + \Delta y) &\approx f_y(x, y) + \Delta y f_{yy}(x, y) + \Delta x f_{xy}(x, y) + \Delta x \Delta y f_{xyy}(x, y).
\end{aligned}
\tag{6.9}
$$

where we assume that the third-order derivative $\Delta x \Delta y f_{xxy}(x, y)$ and $\Delta x \Delta y f_{xyy}(x, y)$ are small enough. Therefore we can get

$$
\begin{aligned}
f_x(x + \Delta x, y + \Delta x) &\approx f_x(x, y) + \Delta x f_{xx}(x, y) + \Delta y f_{xy}(x, y) \\
f_y(x + \Delta x, y + \Delta y) &\approx f_y(x, y) + \Delta y f_{yy}(x, y) + \Delta x f_{xy}(x, y).
\end{aligned}
\tag{6.10}
$$

In the previous section, we defined Δx and Δy as deviations from the sampling peak (0,0). The real peak is located in the $(\Delta x, \Delta y)$, and at the location of the real peak, the first-order derivatives have zero values. Then the problem changes to finding the solution to

$$
\begin{aligned}
f_x(0,0) + \Delta x f_{xx}(0,0) + \Delta y f_{xy}(0,0) &= 0 \\
f_y(0,0) + \Delta y f_{yy}(0,0) + \Delta x f_{xy}(0,0) &= 0.
\end{aligned}
\tag{6.11}
$$

The partial derivative can be built according to the multivariate finite difference formula in [21] as

$$
\begin{aligned}
f_x(x, y) &\approx \frac{f(x + \Delta h) - f(x - \Delta h, y)}{2 \Delta h} \\
f_y(x, y) &\approx \frac{f(x, y + \Delta k) - f(x, y - \Delta k)}{2 \Delta k} \\
f_{xx}(x, y) &\approx \frac{f(x + \Delta h, y) + f(x - \Delta h, y) - 2f(x, y)}{\Delta h^2} \\
f_{yy}(x, y) &\approx \frac{f(x, \Delta k + y) + f(x, y - \Delta k) - 2f(x, y)}{\Delta k^2} \\
f_{xy}(x, y) &\approx [f(\Delta h + x, \Delta k + y) + f(x + \Delta h, y + \Delta k) \\
&\quad - f(x + \Delta h, y - \Delta k) - f(x - \Delta h, y + \Delta k)]/4 \Delta h \Delta k.
\end{aligned}
\tag{6.12}
$$

Similarly, we pick the matrix with sampling pick in the middle, as shown in Figure 6.7. Set $x = 0$ and $y = 0$ and introduce (6.12) to (6.11), then we can obtain the deviation Δx and Δy.

D1	D2	D3
(-1,-1)	(-1,0)	(-1,1)
D4	D5	D6
(0,-1)	(0,0)	(0,1)
D7	D8	D9
(1,-1)	(1,0)	(1,1)

Figure 6.7: Data points matrix

Comparison and selection

Based on the above equations, we can observe that both approximation techniques aim to transform the sampled data into a continuous curve and then find the location where the first-order derivative equals zero. Polynomial fitting requires more data points to achieve sufficient accuracy, while Taylor expansion requires more complex calculations. In the end, both methods result in similar estimates. In this thesis, to simplify the algorithm, we selected the first method.

6.3.3   Direction mapping

The direction of the beam can be calculated by first transforming the beam position to the phase angle difference as

$$
\begin{aligned}
phase_x &= mod((x + \Delta x) \times 360/Nos_x, 360) \\
phase_y &= mod((y + \Delta y) \times 360/Nos_y, 360),
\end{aligned}
\tag{6.13}
$$

where $phase_x$ and $phase_y$ represent the phase difference in the horizontal and vertical dimensions. Nos_x and Nos_y show the size of the matrix after oversampling. Then we map the phase differences into the beam directions, the process is similar to Section 2.4 as

$$
\begin{aligned}
dir_x &= arcsin(phase_x/(360 \times dx)) \times 180/\pi \\
dir_y &= arcsin(phase_y/(360 \times dy)) \times 180/\pi,
\end{aligned}
\tag{6.14}
$$

where dx and dy are the distances between the two antennas in the horizontal and vertical dimensions, respectively, with $dx = 0.513\lambda$ and $dy = 2.03\lambda$. For each SRS slot, the direction mapping process will be repeated eight times for four UEs with two layers.

6.4   Analysis for $B1$, $B5$, $B6$, $B9$

From Table 5.3, in which $B1$, $B5$, $B6$, and $B9$ are measured, we can find the four UEs, receive powers as estimated, so we start with this combination. Initially, we generated scatter plots for the four UEs with two layers. It is essential to emphasize that the focus lies on the phase differences between two antennas; hence, it is necessary to compensate for the original phase added to the first antenna to give a reference phase of 0 degrees, and all the following complex values are compensated automatically. From Figures 6.8 and 6.9, it can be seen that part of the phases applied on the antennas have large deviations from the expected values. As a result, these deviations contribute to errors in the beamforming directions in Figure 6.10.
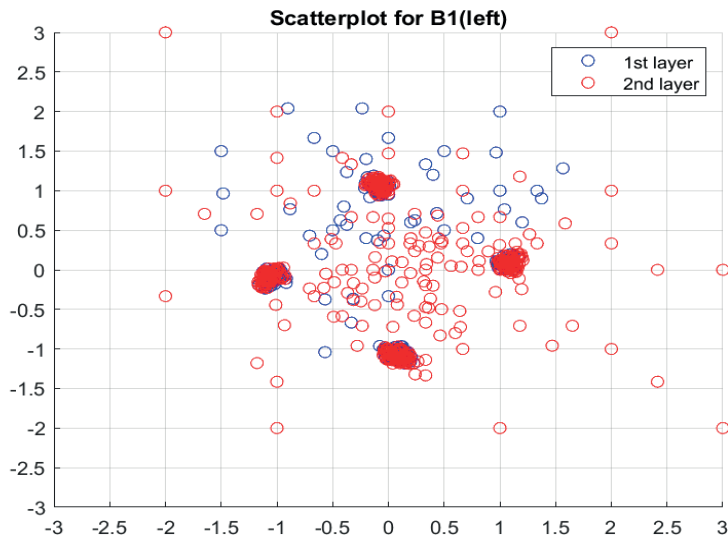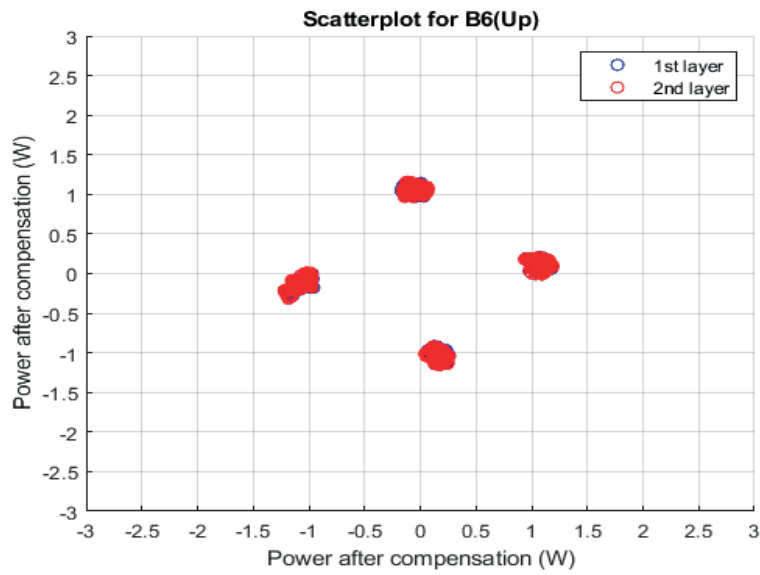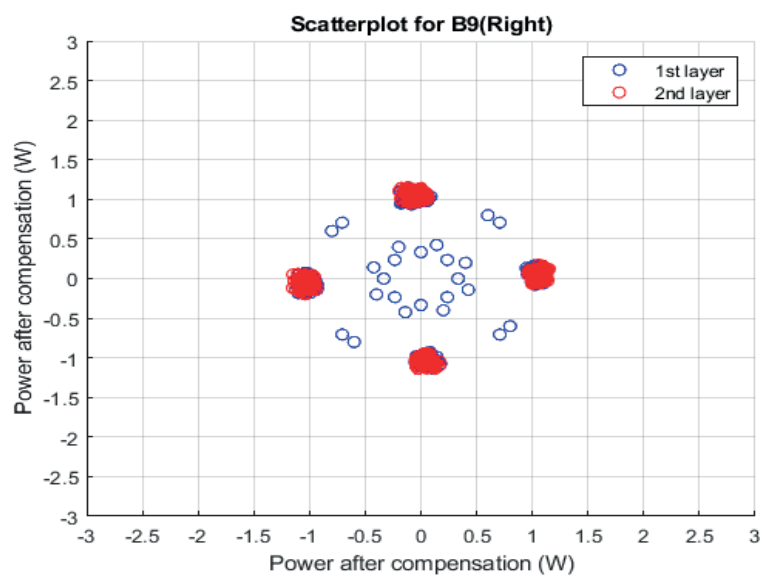
(a) Scatterplot for B1
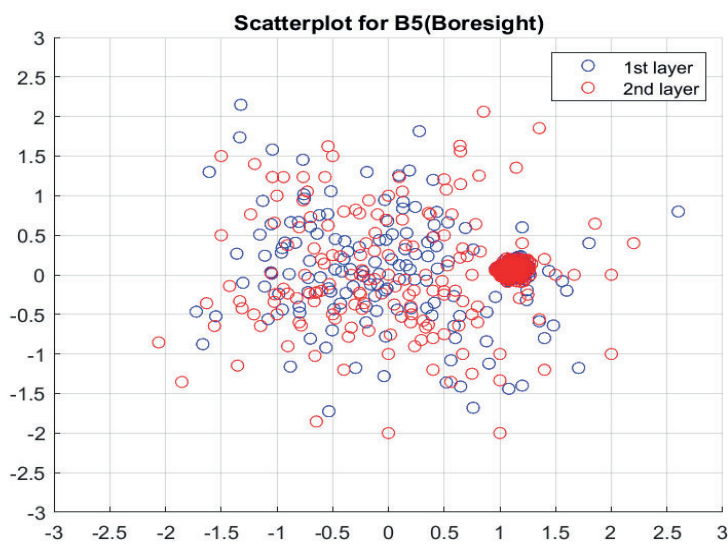
(b) Scatterplot for B5

Figure 6.8: Phase scatterplots for B1 and B5 directions
before filtering
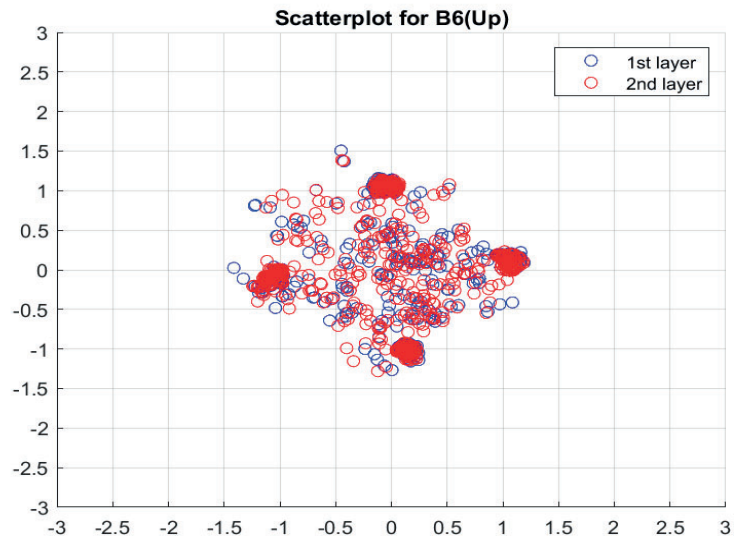
(a) Scatterplot for B6
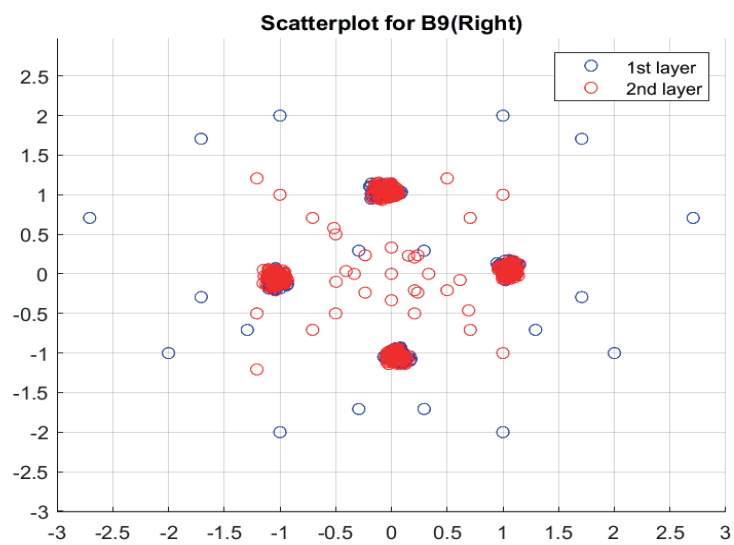
(b) Scatterplot for B9

**Figure 6.9:** Phase scatterplots for B6 and B9 directions before filtering
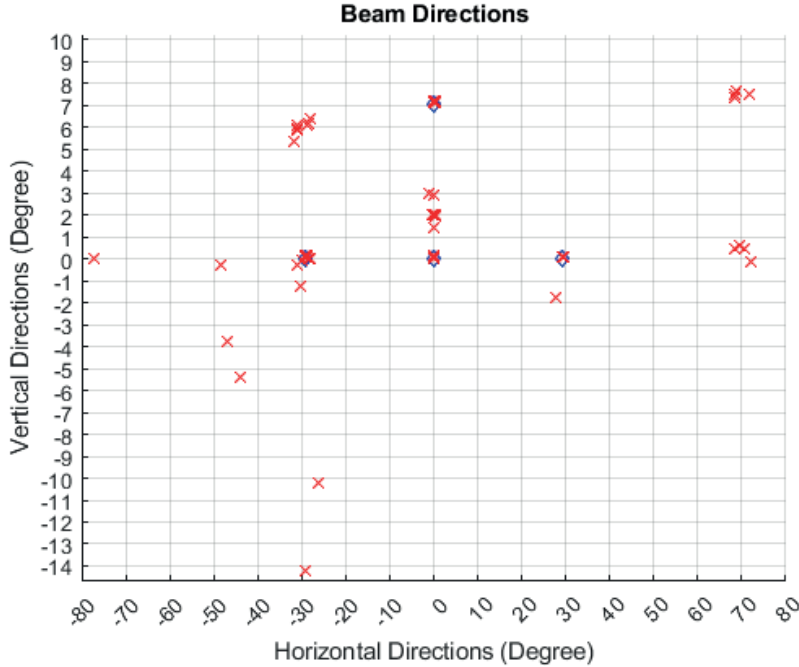
Figure 6.10: Beam directions for B1, B5, B6 and B9

6.5   Trouble-shooting and refinement

Troubleshooting is commonly used to locate the error in the system as observed from the measurements. According to the measurements of the DL SU-MIMO mode, the 2UE-MIMO mode, and the 4UE-MIMO mode mentioned above, we can observe that the possibility of error increases with the increase in the number of UEs. For the first two modes, we cannot identify an obvious error from the measurements; however, for 4UE-MIMO, the errors are magnified and result in a lower received power or a larger EVM in the DL data transmission.

To detect errors in the Butler matrix, we should first ensure that the measurement data from the DU are reliable and errors happening in the DU should be avoided. Because the measurements were conducted under laboratory conditions involving two systems, the errors originate from either the DU or the Butler matrix. To exclude the possibility that errors in the DU influence the troubleshooting for the Butler matrix, we analyzed the trace received for the combinations of $B1$, $B5$, $B6$ and $B9$ and first compensated for the error.

6.5.1   Data cleaning and pre-processing

From the SRS table shown in Table 6.1, we can observe that 64 weights are collected on the antennas for two polarizations per layer. However, according to the

previous chapters, we only have 32 phase shifters corresponding to 32 antenna ports in the AAS per polarization, so not all 64 weights received are used to calculate directions. We only chose 32 (one polarization) of the 64 SRS weights to obtain accurate channel estimation for each layer. The parameters following the layer indicate which polarization to pick for channel estimation; layer = 0 shows weight 1-32 in one polarization used for one layer. Similarly, layer = 1 shows weight 33-64 in another polarization used for the second layer. The next step is filtering out the data that cannot be used for channel estimation, which includes two cases.

- Case1: No data received in the SRS.

- Case2: More than one peak received in one SRS.

Trace ID	bbUeRef	SCG	Layer	Weights(1-8)	Weights (9-16)	...	Weights (57-64)
BFC***.371	0x00001160	68	0	[w1,w2,...,w8]	[0,...,0]	...	[0,...,0]
BFC***.371	0x00001160	68	0	[0,...,0]	[w9,...,w16]	...	[0,...,0]
...	...	...	...	...	...	...	...
BFC***.371	0x00001160	68	0	[0,...,0]	[0,...,0]	...	[w57,...,w64]

Table 6.1: SRS table

According to the SRS forms in Table 6.1, each UE has eight rows in one SRS. Due to an issue that occurred in the DU while processing the multiple UE measurements, there is a likelihood that only a part of the SRS data is received, resulting in a mix of data from one UE with the following one. Consequently, this results in the absence of a peak or the occurrence of multiple peaks within one UE's beam space. Based on these two cases, we implemented a filtering algorithm to filter out the wrong data received and print the warnings showing the ID of erroneous SRS. The flow chart for cleaning data is shown in Figure 6.11.
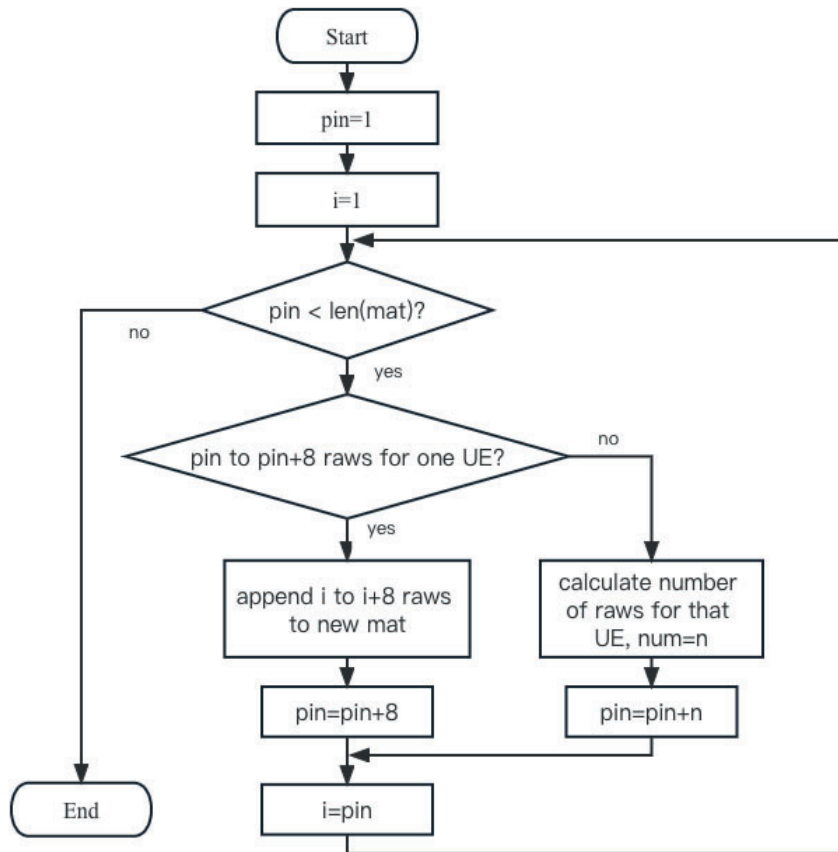
Figure 6.11: Flow chart for data cleaning

6.5.2 Result after data cleaning

After the cleaning of the data, we generate the scatter plots for $B1$, $B5$, $B6$, and $B9$, shown in Figures 6.12 and 6.13. The beamforming directions are shown in Figure 6.14. The beamforming simulation graph is shown in Figure 6.15. From the figures we can conclude that the filter implemented can filter out most of the erroneous SRS collected in the traces. In the following, we focus on the combination of $B1$, $B4$, $B5$, and $B9$.
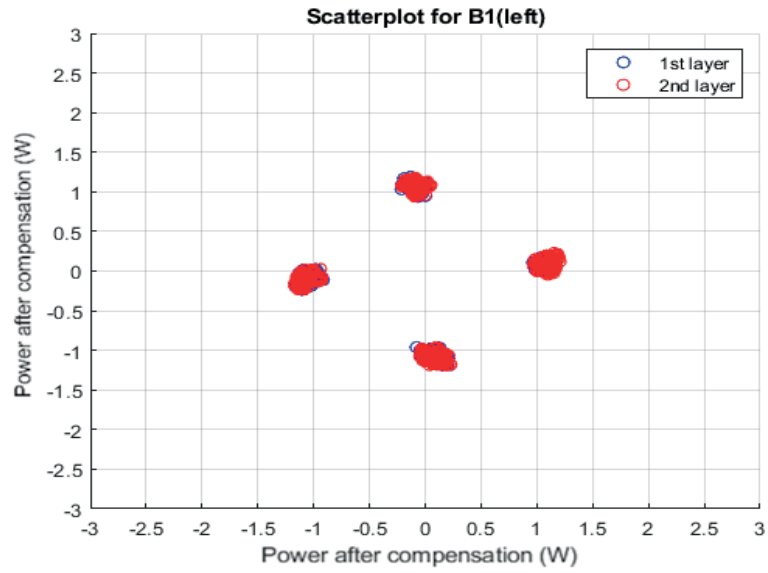
(a) Scatterplot for B1
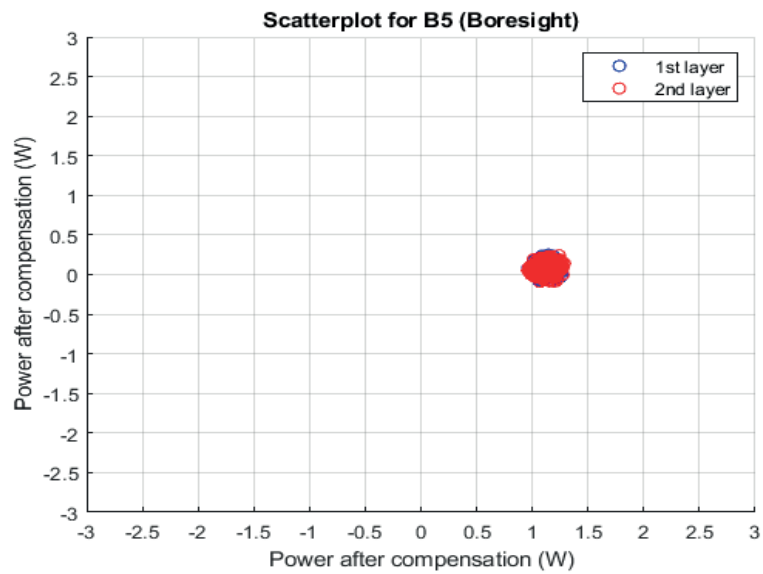
(b) Scatterplot for B5

Figure 6.12: Phase scatterplots for B1 and B5 directions after filtering

(a) Scatterplot for B6

(b) Scatterplot for B9

Figure 6.13: Phase scatterplots for B6 and B9 directions after filtering
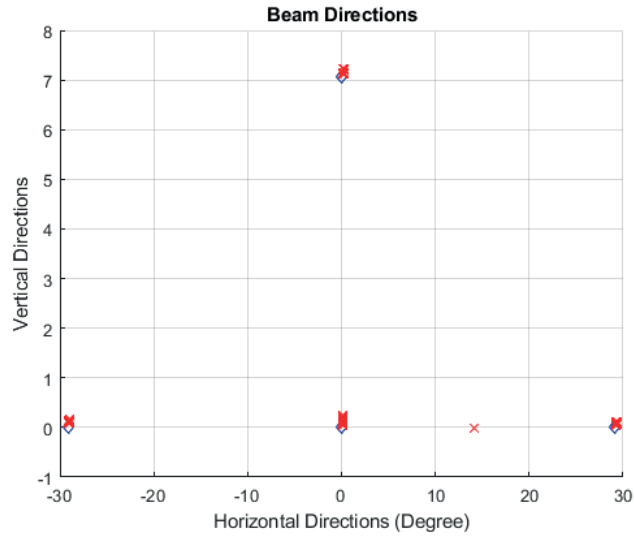
Figure 6.14: Beam directions for B1, B5, B6 and B9

6.6 Butler matrix analysis

From the measurements, we notice that the combination of $B1$, $B4$, $B5$ and $B9$ shows lower power and a larger EVM. To find the root cause of the problem, we generated scatter plots for this combination. The beam pattern generated according to the ideal Butler matrix is shown in Figure 6.16. The noise floor is shown in Figure 6.17 and and we find that the noise floor is stable and fluctuates around 1 mW; this is because the Butler matrix is made of wires and phase shifters, so the signal isolation between those wires is high but not perfect. The influence of the Butler matrix does not change with time, and the noise floor and leakage are also static.
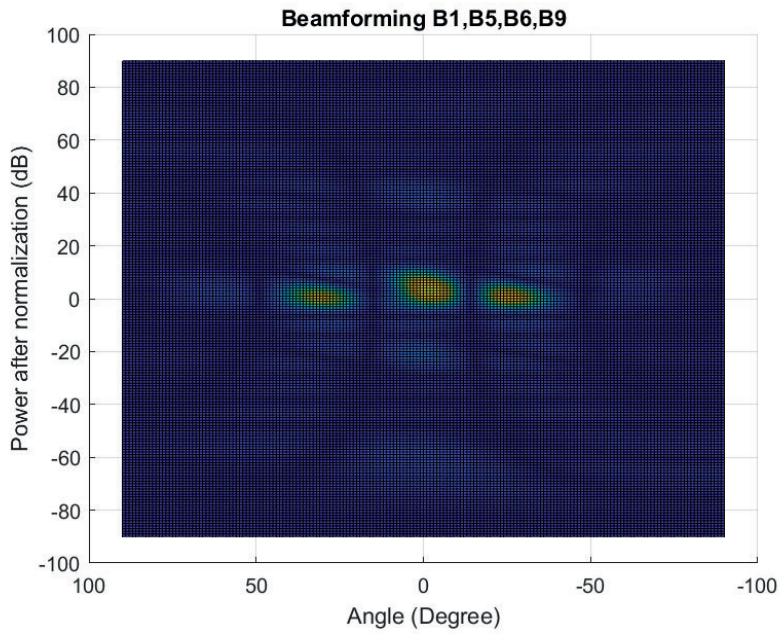
(a) Vertical view for B1,B5,B6,B9
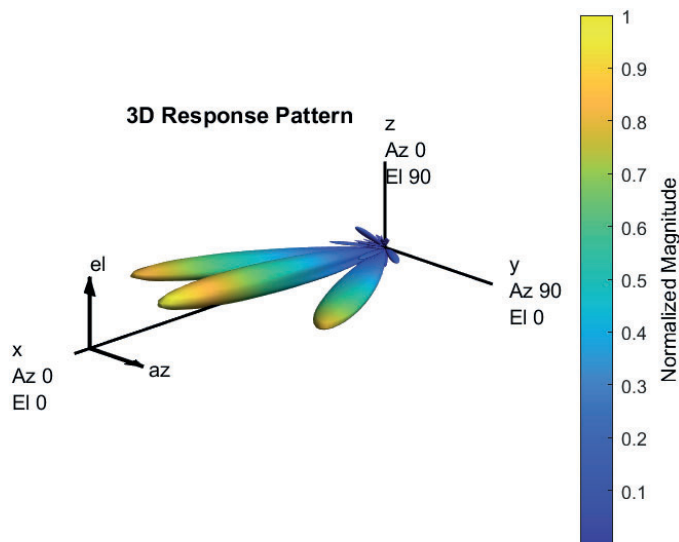
(b) Beam pattern (3D view) for B1,B5,B6,B9

Figure 6.15: Beam pattern for B1,B5,B6,B9
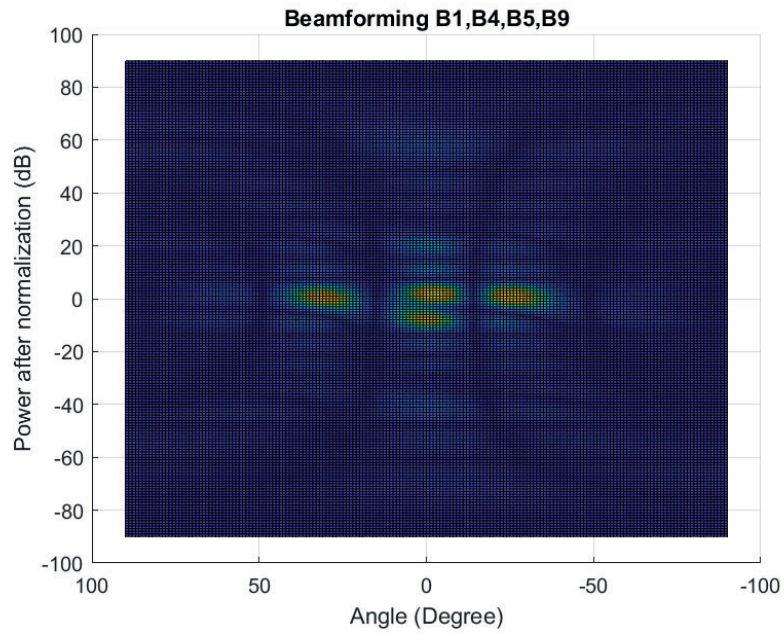
(a) Vertical view for B1,B4,B5,B9
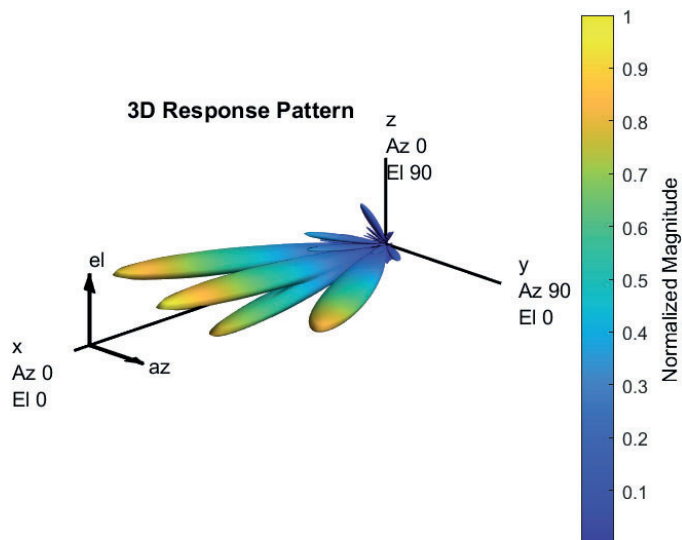
(b) Beam pattern (3D plot) for B1,B4,B5,B9

Figure 6.16: Beamforming for B1,B4,B5,B9
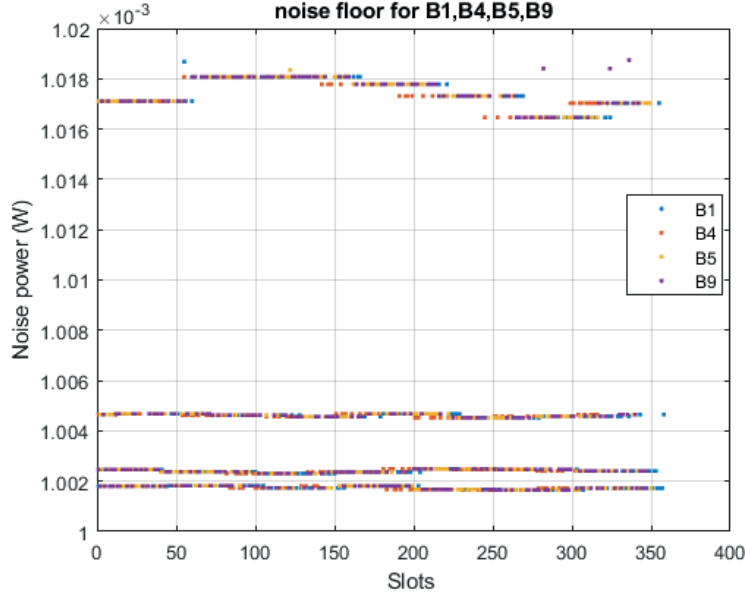
Figure 6.17: Noise floor for B1,B4,B5 and B9

Figures 6.18 and 6.19 show the scatterplots for $B1$, $B4,B5$ and $B9$ directions. Figure 6.20 shows the phase change over time. Referring to Figure 6.19(a) and the second plot in Figure 6.20, it can be seen that a section of one layer exhibits an unexpected phase shift since the start of the measurement; the mismatch is up to 43°maximum. Instead of both layers fluctuating around 0°phase shifts, a part of the phase shifts applied to the antennas in the second layer are estimated to reach up to 50°. Although this phase variation does not significantly affect the PDSCH power received in the UE, it causes a reduction in the expected throughput value and an increase in the EVM in the $B5$ direction.

Upon analyzing Figure 6.18(b) closely, it is apparent that the issue is related to the lower PDSCH power received in the UE in the $B4$ direction. Notably, all the phase shifts intended to be at 270°in the first layer exhibit an additional 40°of phase shift and fluctuate around 310°, while part of phase shifts supposed to be 0°in the first layer has another 50°of phase changes, resulting in -50°. This phase shift leads to a substantial reduction in the power of PDSCH that does not support effective data transmission.
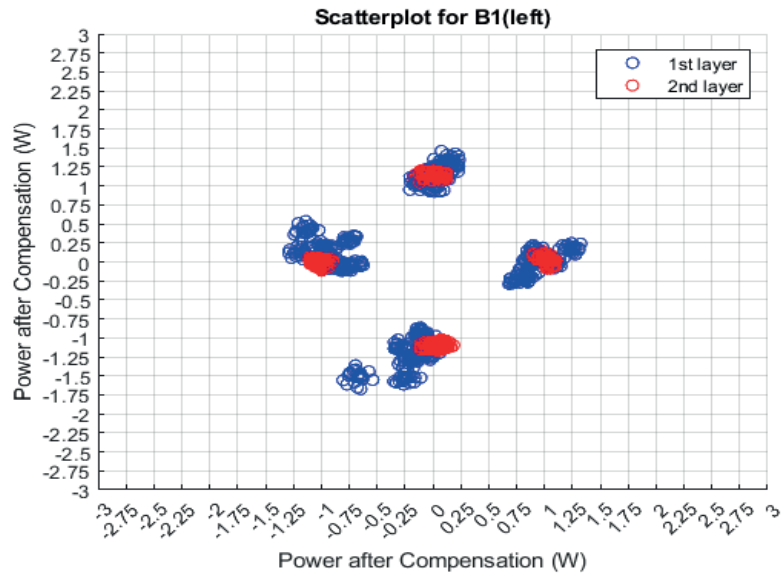
(a) Scatterplot for B1
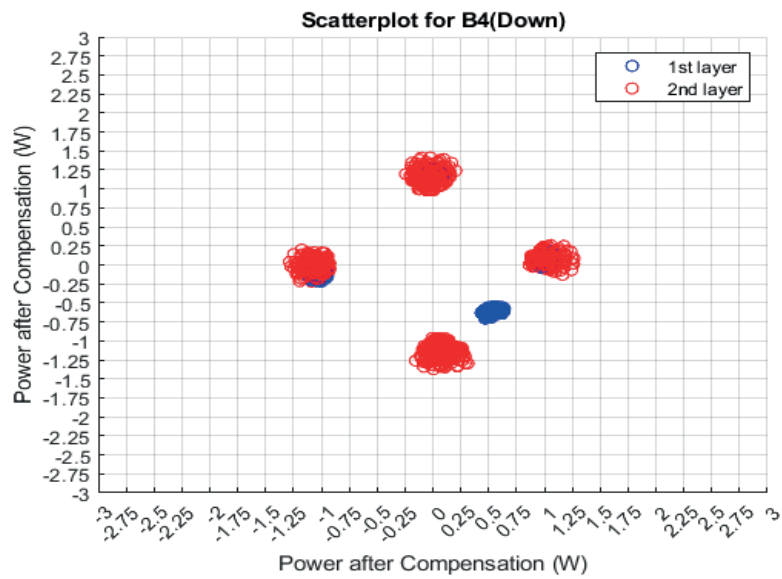
(b) Scatterplot for B4

Figure 6.18: Scatterplots for B1 and B4
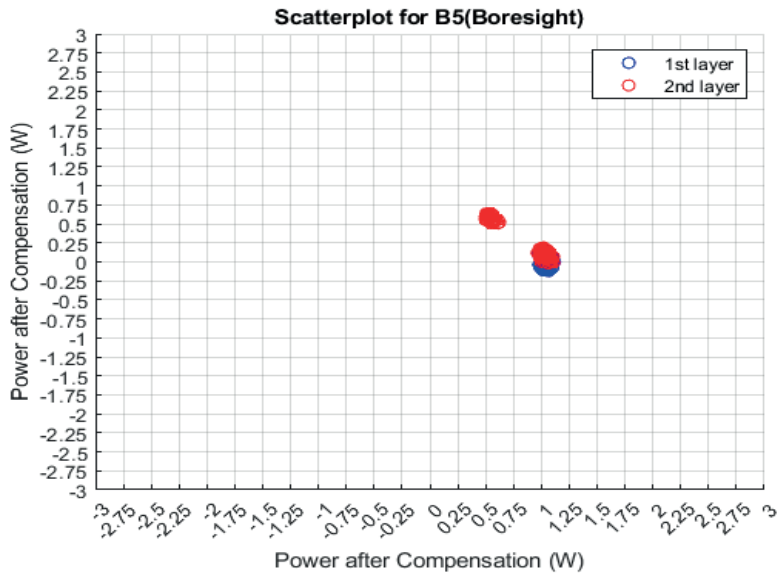
(a) Scatterplot for B5
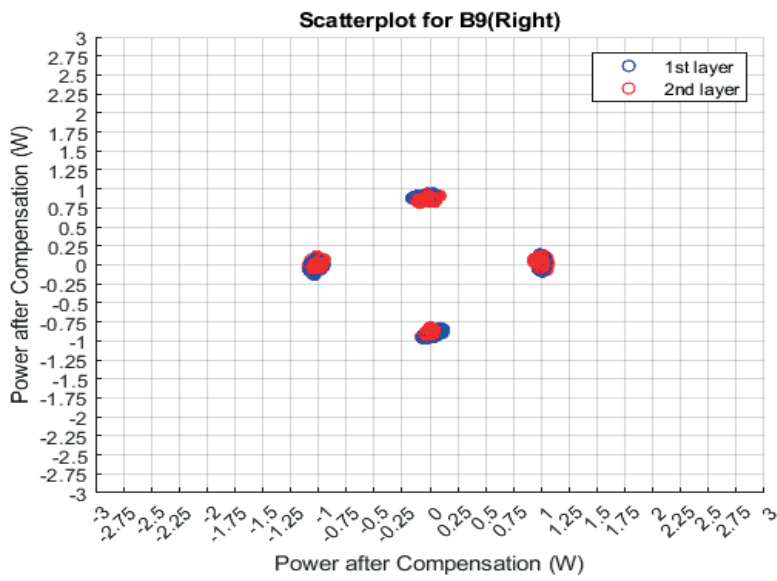
(b) Scatterplot for B9

Figure 6.19: Scatterplots for B5 and B9
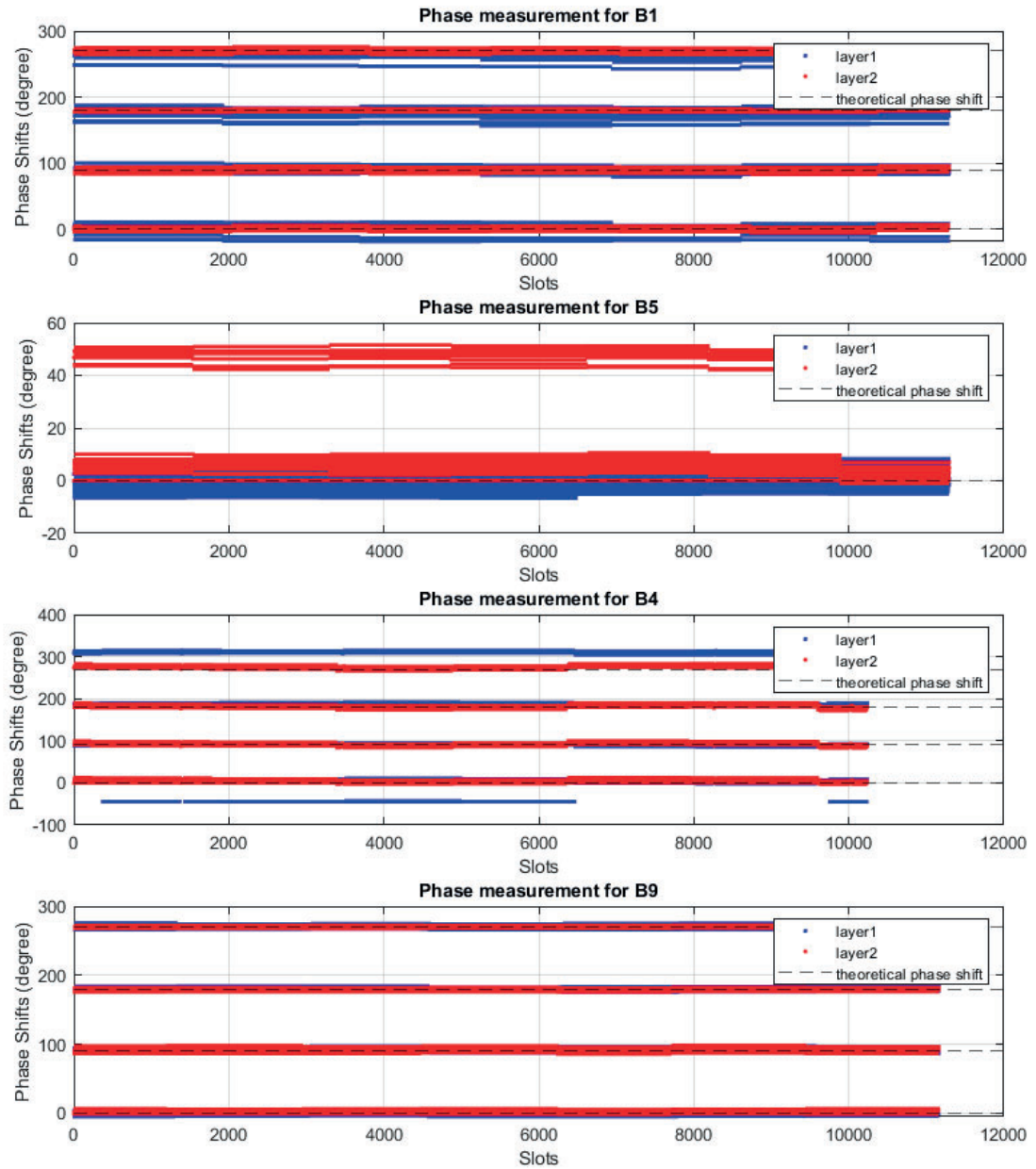
Figure 6.20: Phase shifts for B1, B4, B5 and B9

As a result, the expected throughput value practically degrades to inadequate throughput in the $B4$ direction. Then we plot the Figure showing how the estimated beam directions change with time. The plots are shown in Figures 6.21 and 6.22.

From the beamforming direction estimation plots, we can notice that for the combination of $B1$, $B4$, $B5$, and $B9$, both the horizontal and vertical deviations from the ideal peak are less than 1°for the whole measurement period. The deviation for the $B4$ direction, which receives less power than other directions, is continuously estimated to be less than 5°. The beam mapping plot for $B1$, $B4$, $B5$, and $B9$ is shown in Figure 6.23. From Figure 6.20, we find that the deviation in the horizontal and vertical directions is within 0.15°compared to the expected angle. However, for the $B1$ direction, the beam angle from the expected value in the horizontal direction is up to 0.35°.
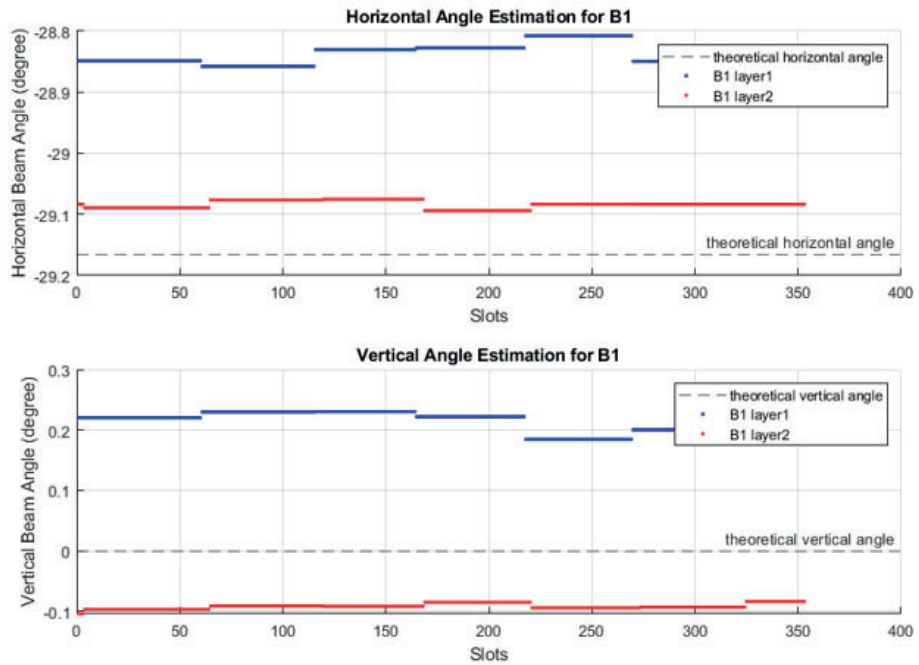
(a) Peak estimation for B1
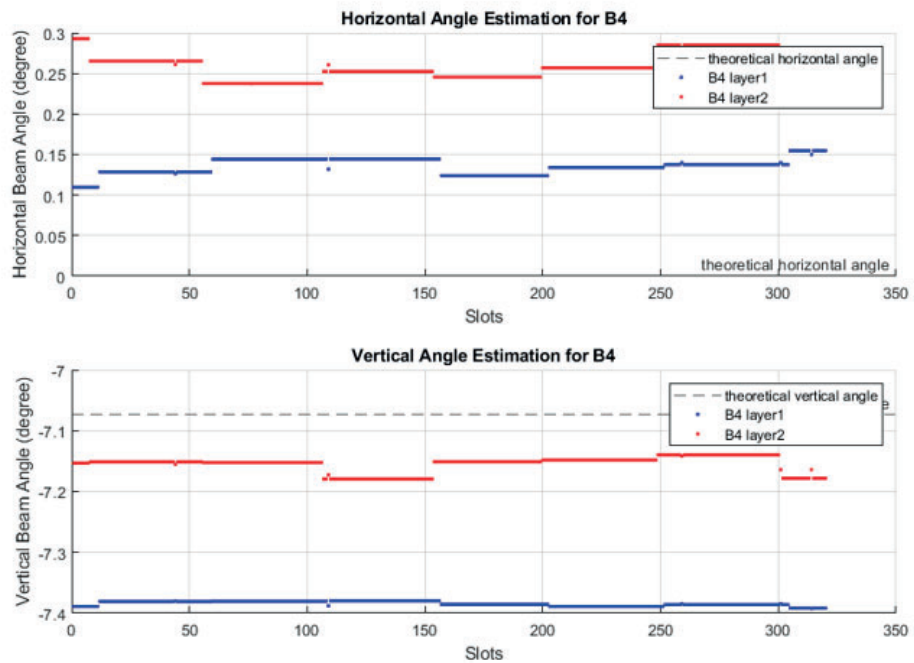
(b) Peak estimation for B4

Figure 6.21: Peak estimations for B1 and B4
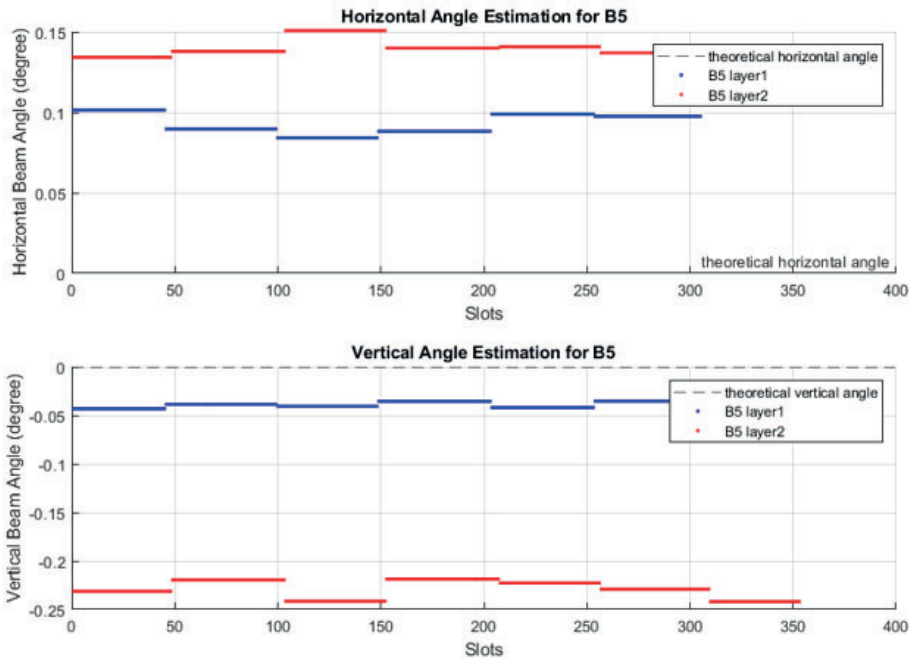
(a) Peak estimation for B5
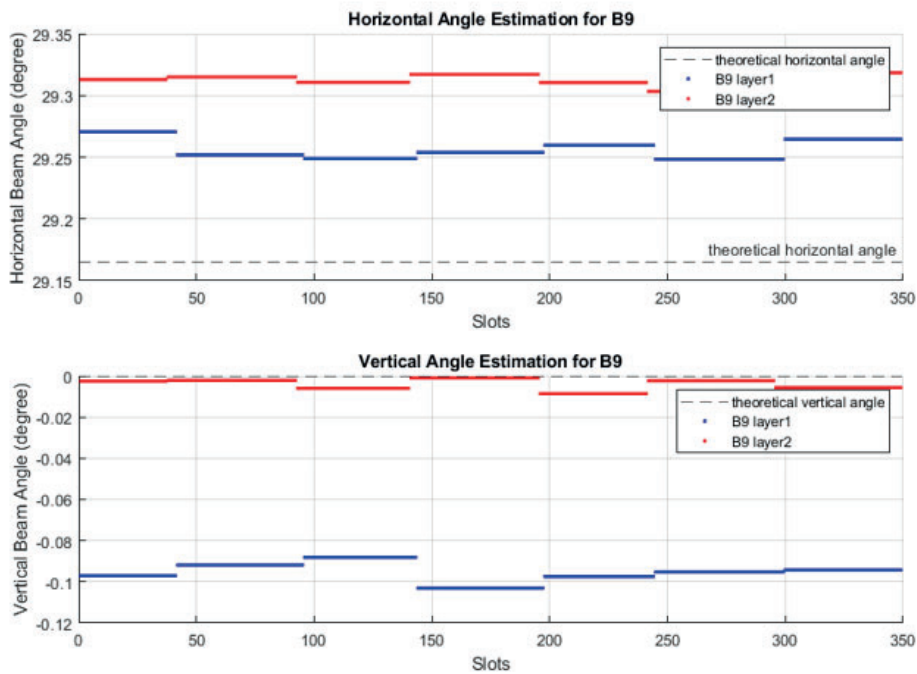
(b) Peak estimation for B9

Figure 6.22: Peak estimations for B5 and B9
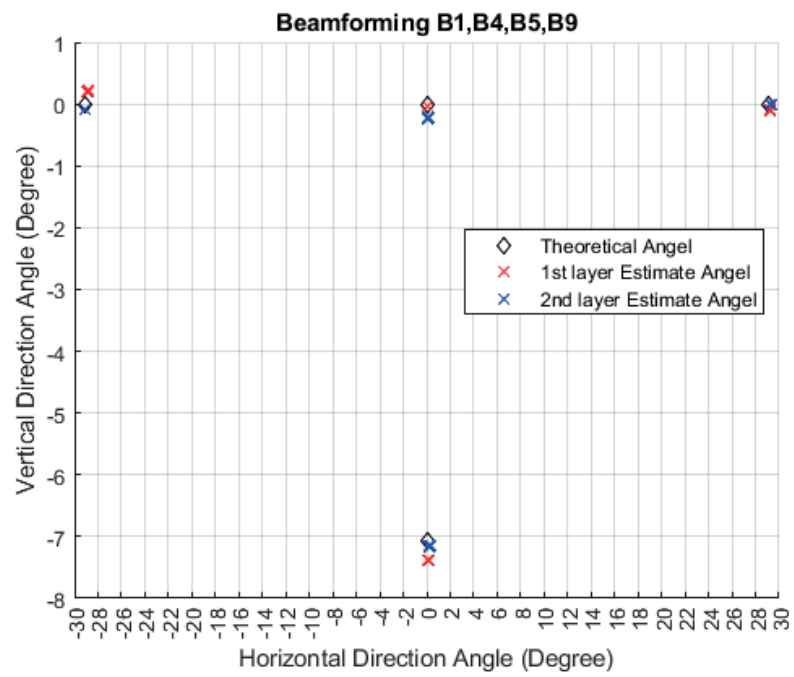
Figure 6.23: Beam directions mapping for B1, B4, B5 and B9

Conclusion and Future work

7.1 Summary

This thesis focuses on investigating a reciprocity-based MU-MIMO test system, we analyze a new method for combining UL and DL measurement data and visualize the data processing steps to facilitate troubleshooting. The motivation is to change the situation that relies only on DL power measurements for system evaluation and troubleshooting.

Firstly we build a mathematical model for the Butler matrix, which is used to provide phase shifts to simulate AOA in the UL and reversely to change phase shifts applied on antennas to direct power in the DL. The purpose is to derive the ideal phase information for MIMO to form beams in specific directions. Then, based on the measurements of both UL and DL transmissions, we identify the multi-user combination which shows unexpected output to troubleshoot. Subsequently, we processed the data obtained from SRS to identify the source of the problems and how those problems in the Butler matrix can influence the test result. Additionally, we use an ideal Butler matrix model to simulate the process that occurred in the lab and compare it with the measurement data to make the troubleshooting process simpler. To ensure that the results are stable, the measurement for one combination is repeated three times to exclude the effect of uncontrollable incidents.

Based on our investigation, we identified two main problems that exist in this lab system which can lead to unexpected test results. The first issue is the data processing in DU, the writing speed is faster than the reading speed in the CPU which causes crush traces in DU. As a result, an SRS will mix with the following one and channel estimation information for two UEs will combine and show up as one UE estimation. After implementing a filter algorithm to perform data cleaning, problems can be solved. The second issue is the phase error given by the Butler matrix, which can influence the DL measurement results and beamforming direction deviations. The phase error generated by the Butler matrix will lead to mismatches with the antennas, thus the expected power cannot be received by the UEs in the DL because of the power leakage and beam direction shift. Conclusions drawn based on the effect of these two problems on our system performance are presented in the next section.

7.2   Conclusions

Based on our investigation, we designed a new measurement method to test the effectiveness of the Butler matrix, which satisfies the goal of our thesis, and some conclusions are drawn based on the investigation. First, a phase-shift error can influence the DL measurement results to varying degrees. Part of phase mismatches in one layer of a UE will result in larger EVM and reduced throughout, whereas the DL received power in DL will fluctuate around the expected value. Continuous erroneous phase shifts in one layer in every slot lead to failure in measurements. Phase mismatches within 25°have a negligible impact on DL thanks to automatic antenna calibration in the system. However, if any of the four fixed phase differences provided by the Butler matrix undergoes an erroneous phase shift and the phase errors are larger than 50°, these mismatches between the theoretical phase vector and real phase applied on antennas will continuously influence the PDSCH power, which shows a stable lower power and lower throughput than other outputs in measurement.

In particular, the phase mismatch between the antennas and the Butler matrix does not have as significant an impact on beamforming directions as originally expected. The system in the lab shows a strong capability to compensate for small mismatches in beamforming directions. Ports that correspond to the directions of the system with phase mismatches within 15°can keep a beam angle deviation in both horizontal and vertical dimensions to within 0.15°from the expected beamforming direction. For the ports with phase errors from predetermined values provided by the Butler matrix theoretically will lead to larger deviations; however, the deviations fall within an acceptable range of 0.35°.

Based on Figures 6.21 to 6.22, we can find that the system remains stable in the measurement with respect to beam angle changes. The estimated angle fluctuates within the range of 0.05°, which also verified the stability of the system based on the Butler matrix.

7.3   Limitations and future work

The Butler matrix measurement and test topic can be extended and improved in various directions. Here, we list some of the current limitations and refinements that can be made in the future.

- The troubleshooting focuses on the problem of the Butler matrix as well as the transmitting process in the lab system. The Butler matrix processes two layers of each UE separately, so the influence between two Butler matrices can be neglected in our case. We did not consider the influence between two layers from the UE perspective, which would require measurements from the MS. MS measurements cannot be performed because of the limitations of the tools. Therefore, this aspect could be investigated when a suitable tool is available.

- Our test system does not support long-time measurement because the log is too large to process with a laptop, so we only pick the first 2750 Subframe Numbers (SFNs) each time, which lasts about 27 seconds. So we assume that

the reciprocity works well in our lab case. Studying the synchronizations between UL and DL in the system will also be a topic worth further study.

- In lab cases, we assume that the whole bandwidth goes through the same channel, so we only pick SCG 68, which represents the center frequency. This assumption is only valid in laboratory cases. For OTA measurement, we need to collect more SCG to study how channel estimation changes throughout the bandwidth.

- Our code only supports the case that all the UE works, which means that we can at least receive the SRS data from all UEs. If one of the UEs does not work and we cannot receive any SRS for that UE in the UL, then we cannot perform DL transmission for any UE. According to our measurements, sometimes we could not receive any signal from one UE for a while, which resulted in no throughput in the DL. Therefore, the code could be improved to handle this limitation.

Bibliography

[1] A. Paulraj, R. Nabar, and D. Gore. *Introduction to Space-Time Wireless Communications*. Cambridge University Press, 2003. ISBN: 9780521826150. URL: `https://books.google.se/books?id=YQSsoPDfyngC`.

[2] P.H. Lehne and M. Pettersen. "An Overview of Smart Antenna Technology for Mobile Communications Systems." In: *IEEE Communications Surveys and Tutorials, 2, 2-13* 2 (1999), pp. 2–13.

[3] H. Nachouane et al. "Broadband 4x4 Butler Matrix Using Wideband 90° hybrid Couplers and Crossovers for Beamforming Networks". In: Apr. 2014. DOI: `10.1109/ICMCS.2014.6911309`.

[4] A. K. Vallappil et al. "Butler Matrix Based Beamforming Networks for Phased Array Antenna Systems: A Comprehensive Review and Future Directions for 5G Applications". In: *IEEE Access* 9 (2021), pp. 3970–3987. DOI: `10.1109/ACCESS.2020.3047696`.

[5] A. Kalachikov and A. Stenin. "Performance Evaluation of the SRS Based MIMO Channel Estimation on 5G NR Open Source Channel Model". In: *2021 IEEE 22nd International Conference of Young Professionals in Electron Devices and Materials (EDM)*. 2021, pp. 124–127. DOI: `10.1109/EDM52169.2021.9507598`.

[6] C. Linfeng. *Performance Evaluation and Modeling of a Beam-simulation System for MIMO communications*. Lund University, Sweden, Master's thesis report, 2022.

[7] H. Asplund et al. *Advanced Antenna Systems for 5G Network Deployments: Bridging the Gap Between Theory and Practice*. Elsevier Science, 2020. ISBN: 9780128200469. URL: `https://books.google.se/books?id=MWXsDwAAQBAJ`.

[8] JavaLab Science Simulations. *Phase array*. https://javalab.org/en/phase$_a$rray$_e$n/.

[9]   J. Vikstedt. "Test Challenges of Smart Antenna Systems". In: *2017 IEEE International Symposium on Electromagnetic Compatibility Signal/Power Integrity (EMCSI)*. 2017, pp. 1–47. DOI: `10.1109/ISEMC.2017.8078068`.

[10]   P. Kyösti. "Correlation of Hybrid Beamforming Arrays in the Context of OTA Testing". In: *IEEE Antennas and Wireless Propagation Letters* 19.4 (2020), pp. 671–675. DOI: `10.1109/LAWP.2020.2976515`.

[11]   H. Pei et al. "Over-the-Air Testing of 5G Millimeter-Wave System with Adaptive Beamforming". In: *2019 IEEE MTT-S International Wireless Symposium (IWS)*. 2019, pp. 1–3. DOI: `10.1109/IEEE-IWS.2019.8803918`.

[12]   I. Albert, L. Diquelou, and S. D. Souza. "Test Bench for Digital Beamforming Performances Characterization". In: *2012 15 International Symposium on Antenna Technology and Applied Electromagnetics*. 2012, pp. 1–3. DOI: `10.1109/ANTEM.2012.6262346`.

[13]   P. Krishna, T. Anil Kumar, and K. K. Rao. "Multiuser MIMO systems: Spectral and Energy Efficiencies, Estimations and Capacity Limits". In: *2015 Twelfth International Conference on Wireless and Optical Communications Networks (WOCN)*. 2015, pp. 1–6. DOI: `10.1109/WOCN.2015.8064514`.

[14]   Mathworks. *TDD Reciprocity-Based PDSCH MU-MIMO Using SRS*. URL: `https://se.mathworks.com/help/5g/ug/tdd-reciprocity-based-pdsch-beamforming-using-srs.html` (visited on 07/29/2023).

[15]   E. Dahlman, S. Parkvall, and J. Skold. *5G NR: The Next Generation Wireless Access Technology*. Elsevier Science, 2020. ISBN: 9780128223208. URL: `https://books.google.se/books?id=PZH9DwAAQBAJ`.

[16]   M. Cai. *Modeling and Mitigating Beam Squint in Millimeter Wave Wireless Communication*. Ph.D. report, University of Notre Dame, Indiana, United States, 2018.

[17]   AvnetAbacus. *Understanding Advanced Antenna Systems*. 1999. URL: `https://www.avnet.com/wps/portal/abacus/solutions/markets/communications/5g-solutions/understanding-advanced-antenna-systems/` (visited on 07/29/2023).

[18]   H. Ni, Zh. Li, and H. Song. "Moving Least Square Curve and Surface Fitting with Interpolation Conditions". In: *2010 International Conference on Computer Application and System Modeling (ICCASM 2010)*. Vol. 13. 2010, pp. V13-300-V13–304. DOI: `10.1109/ICCASM.2010.5622770`.

[19]   A. Abdulle and G. Wanner. "200 Years of Least Squares Method". In: vol. 57. Springer International Publishing, 2002, pp. 45–60.

[20]   University of Queensland. *Taylor Series in Two Dimensions*. URL: https://teaching.smp.uq.edu.au/scims/Num_analysis/Taylor.html.

[21]   L. M. Milne-Thomson. *The Calculus of Finite Differences*. English. London: Macmillan & Co., Ltd. XIX, 558 S., 23 Fig. (1933). 1933.

Extra material

In this part of the report, we present some graphs in larger sizes, which have been subplotted to prevent having too many graphs in the main chapters.

## A.1 Second measurement for B1, B4, B5 and B9

Figures A.1 and A.2 show the scatter plot of $I + Q$ values for the 4UE combination.
  Figures A.3 to A.6 show the phase changes with time for 4UE.
 Figures A.7 to A.10 show the deviation of beamforming directions.
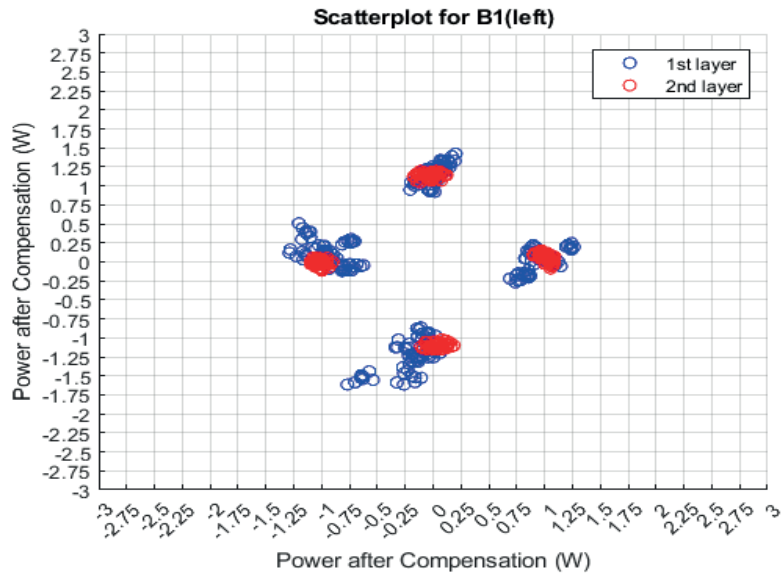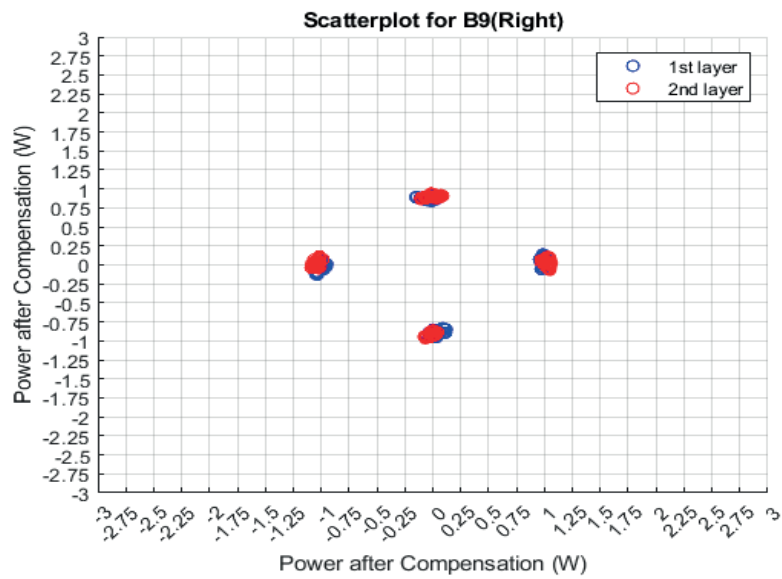
(a) Scatterplot for B1
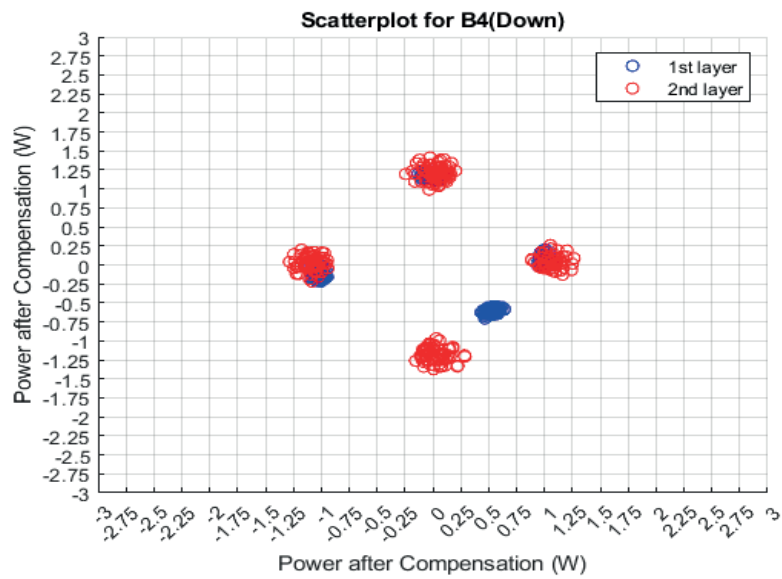
(b) Scatterplot for B4

Figure A.1: Scatterplots for B1 and B4
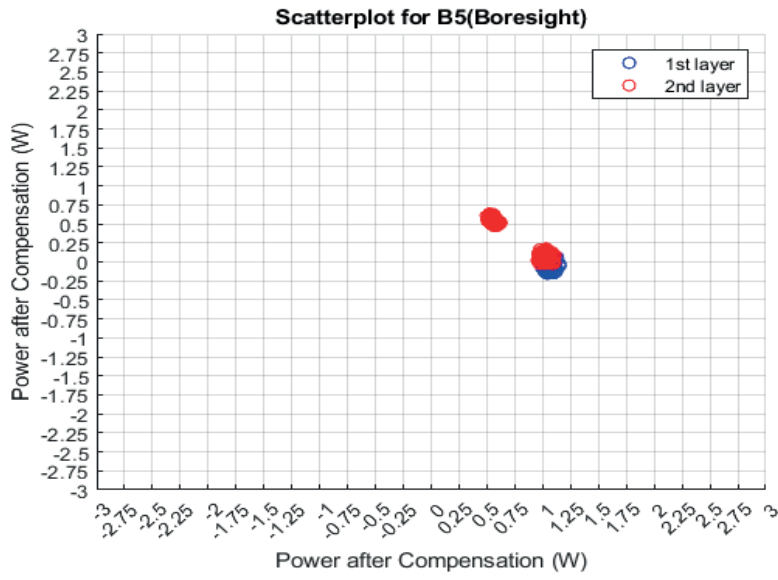
(a) Scatterplot for B5
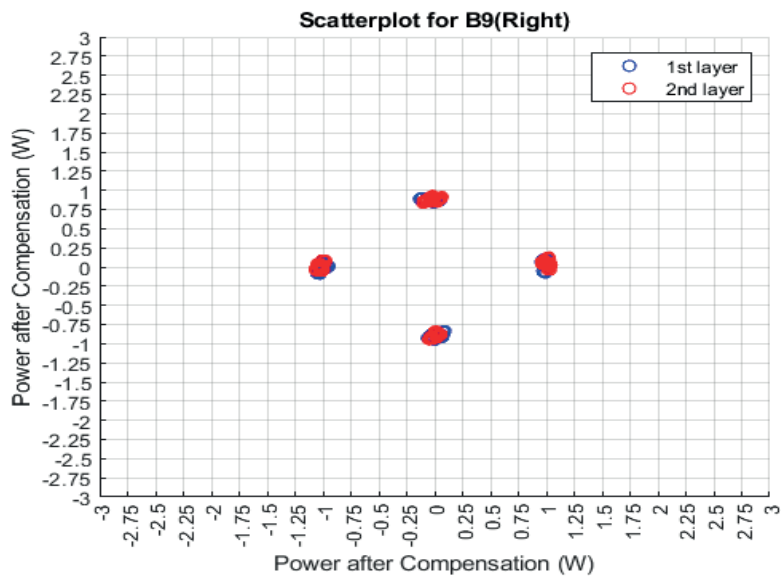
(b) Scatterplot for B9
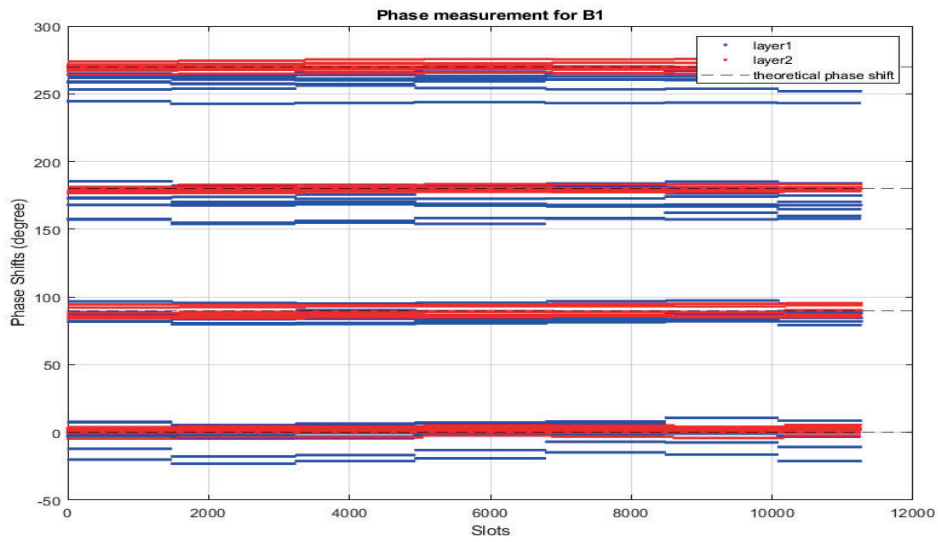
Figure A.2: Scatterplots for B5 and B9
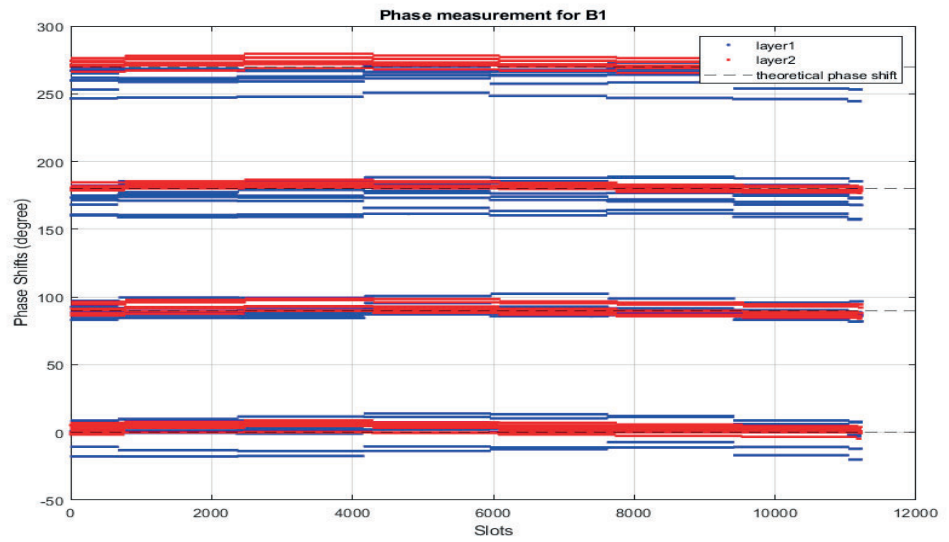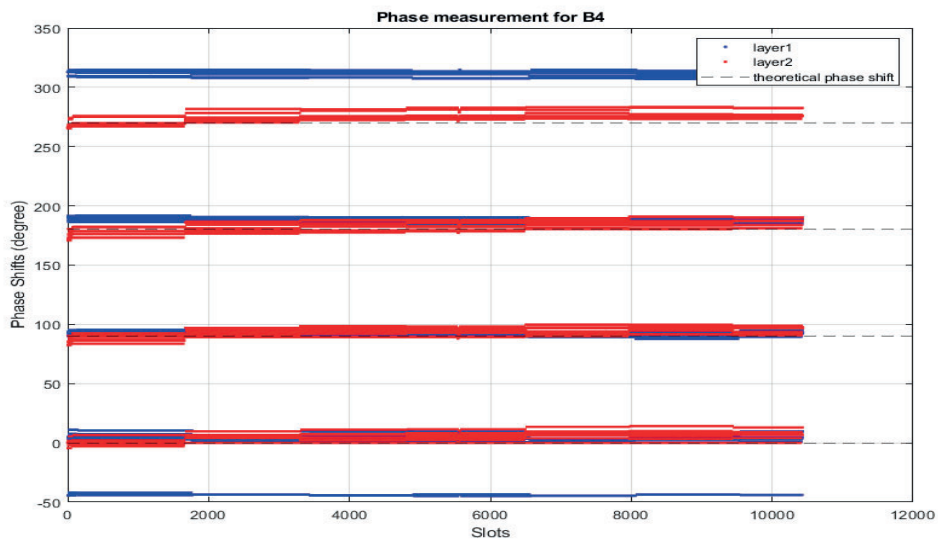
Figure A.3: Phase measurements for B1
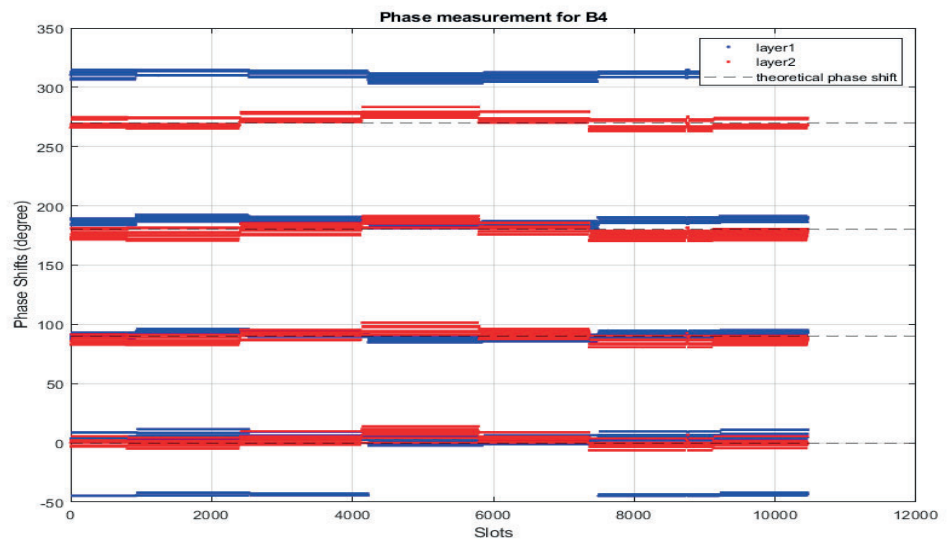
Figure A.4: Phase measurements for B4
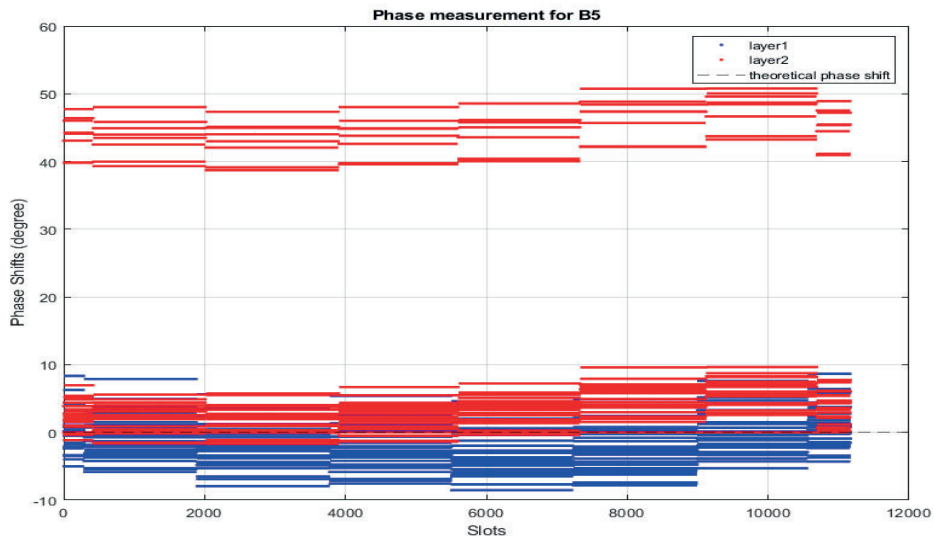
Figure A.5: Phase measurements for B5
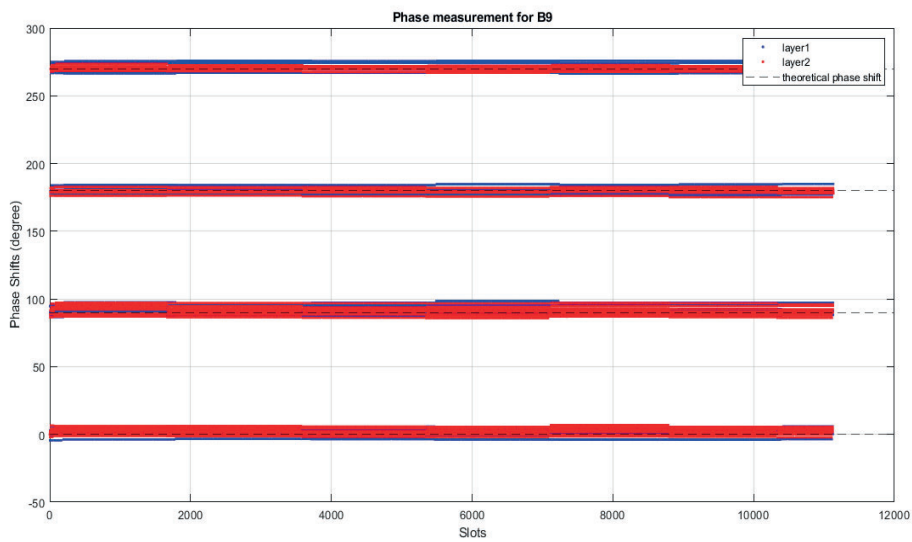
Figure A.6: Phase measurements for B9
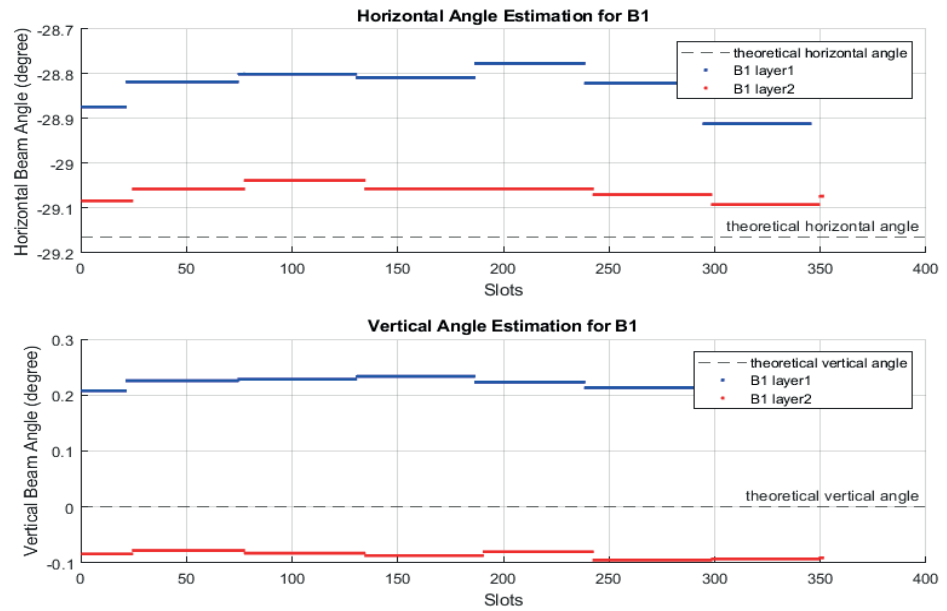
Figure A.7: Peak estimation for B1
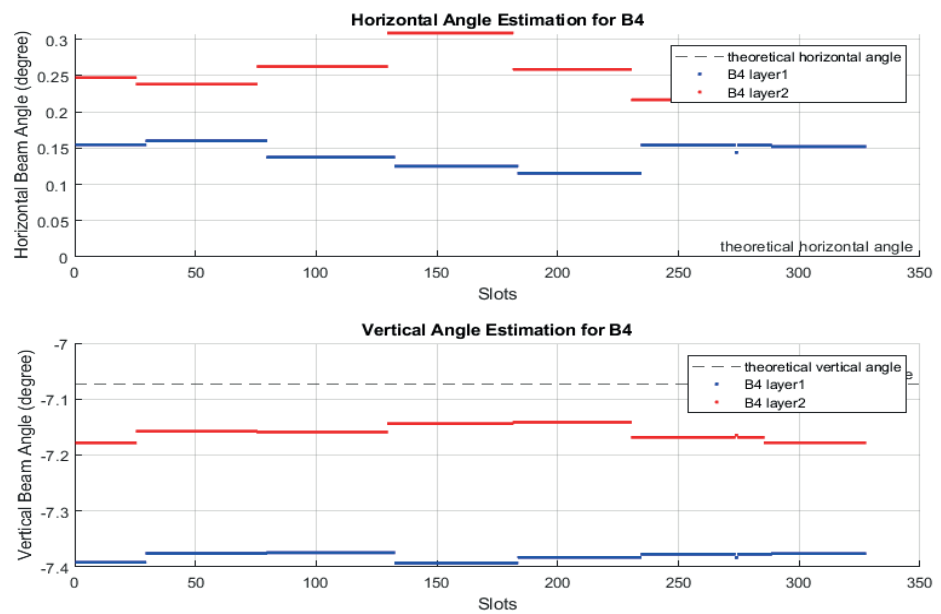
Figure A.8: Peak estimation for B4
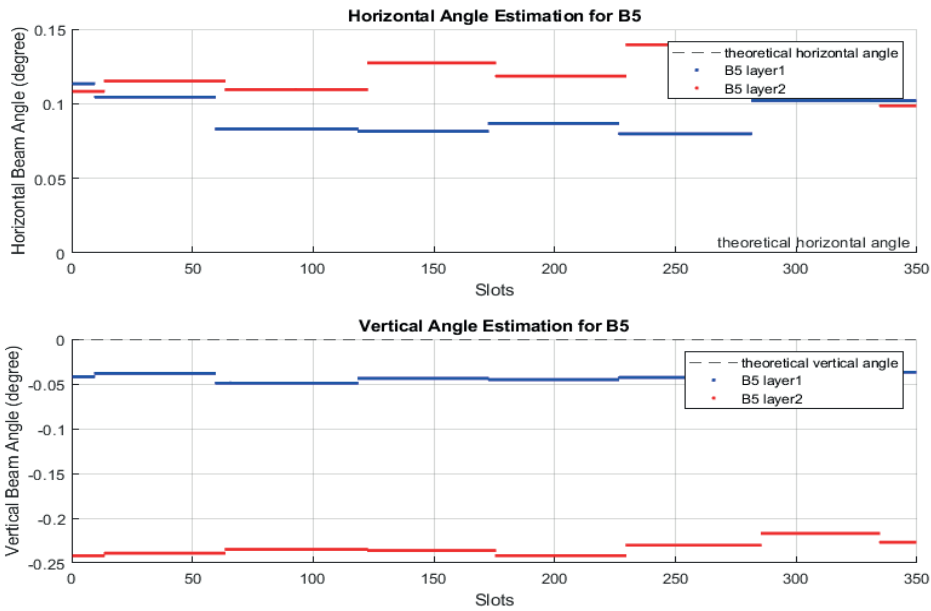
Figure A.9: Peak estimation for B5
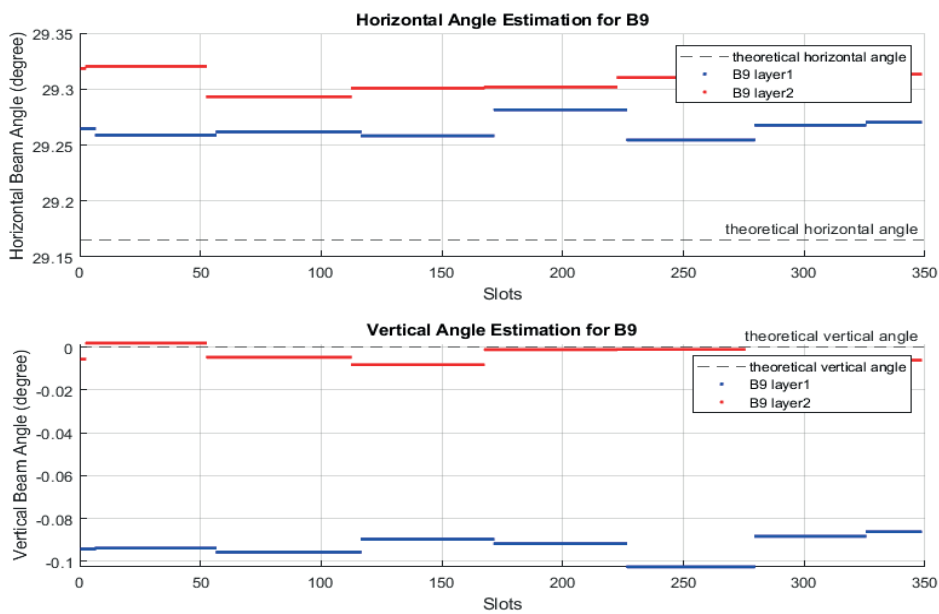
Figure A.10: Peak estimation for B9

A.2 Third measurement for B1, B4, B5 and B9

Figure A.11 and A.12 show the scatter plot of I + Q values for the 4UE combination.

Figures A.13 to A.16 show the phase changes with time for 4UE.

Figures A.17 to A.20 show the deviation of beamforming directions.
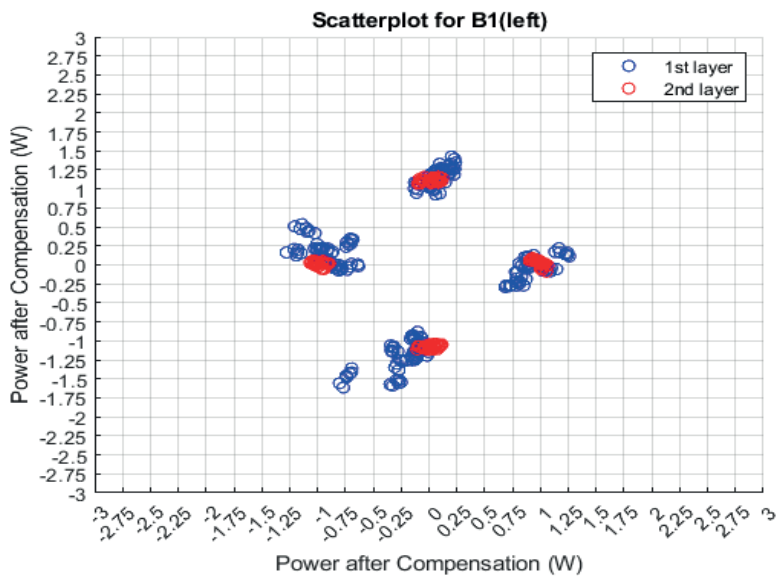
(a) Scatterplot for B1
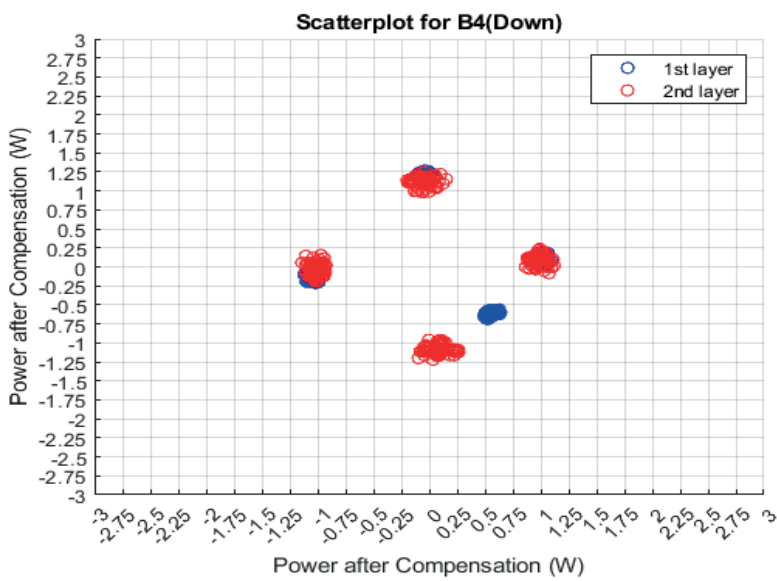
(b) Scatterplot for B4

Figure A.11: Scatterplots for B1 and B4
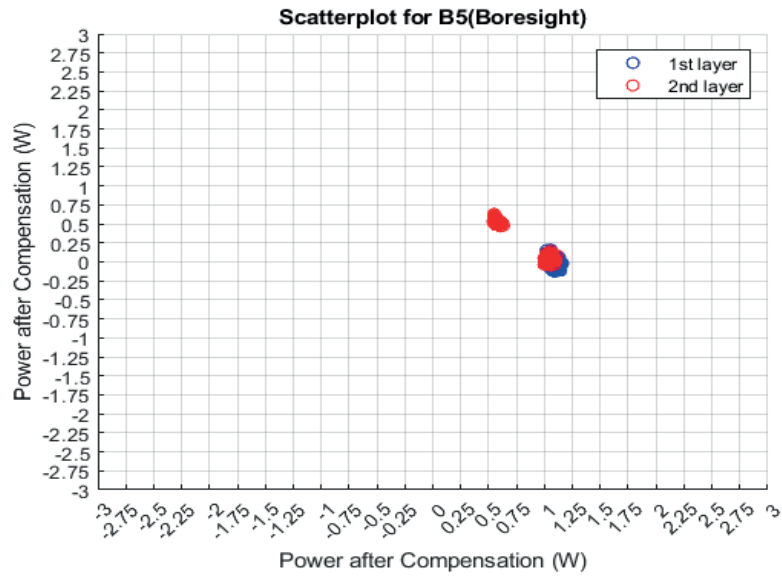
(a) Scatterplot for B5

(b) Scatterplot for B9

Figure A.12: Scatterplots for B5 and B9

Figure A.13: Phase measurements for B1
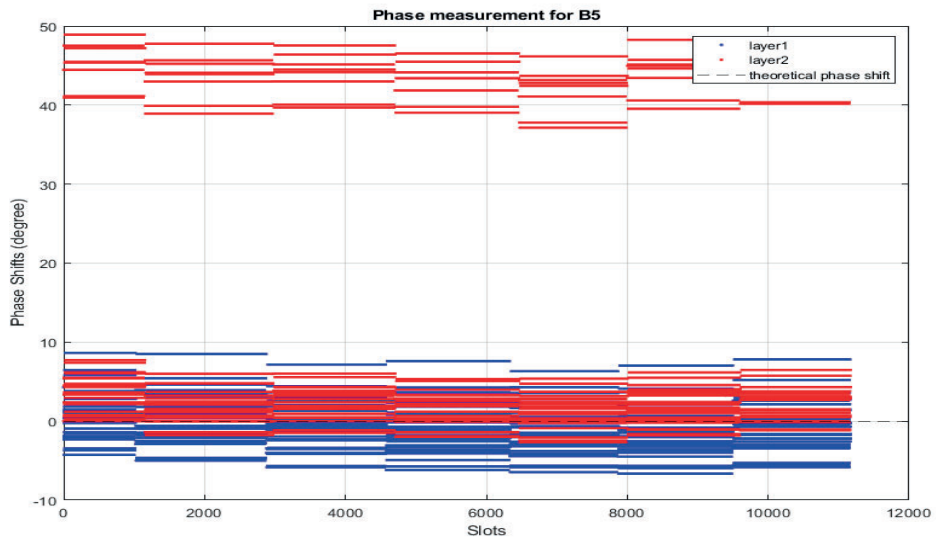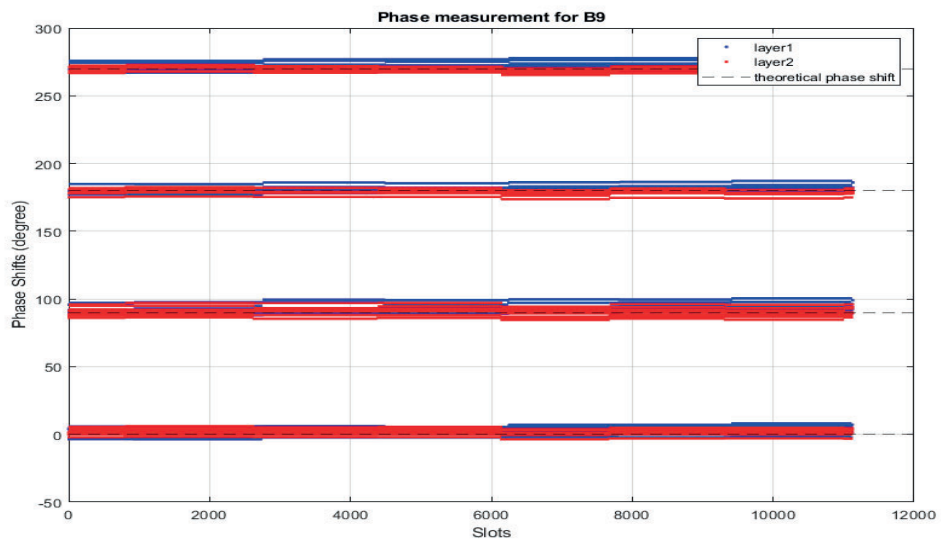

Figure A.14: Phase measurements for B4

Figure A.15: Phase measurements for B5
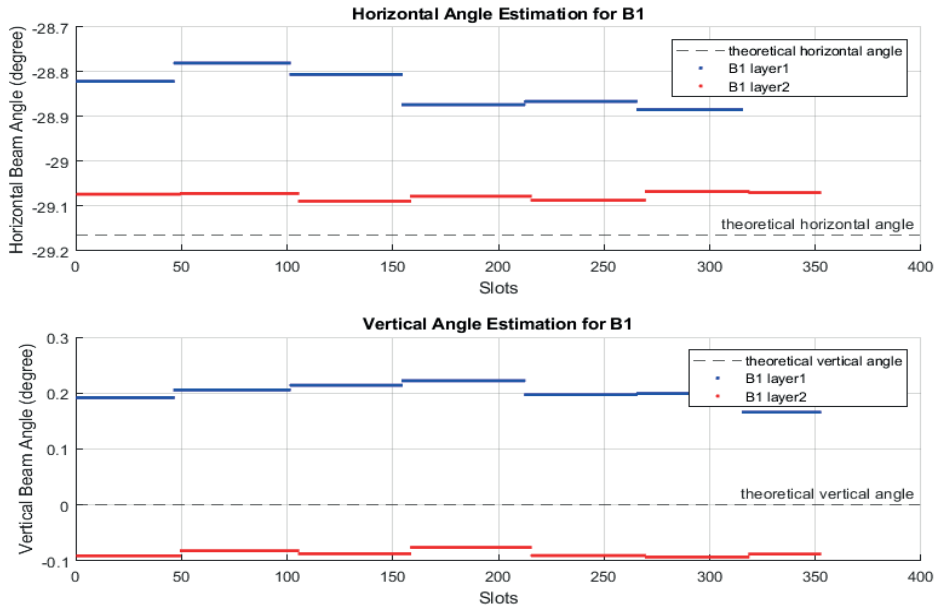

Figure A.16: Phase measurements for B9
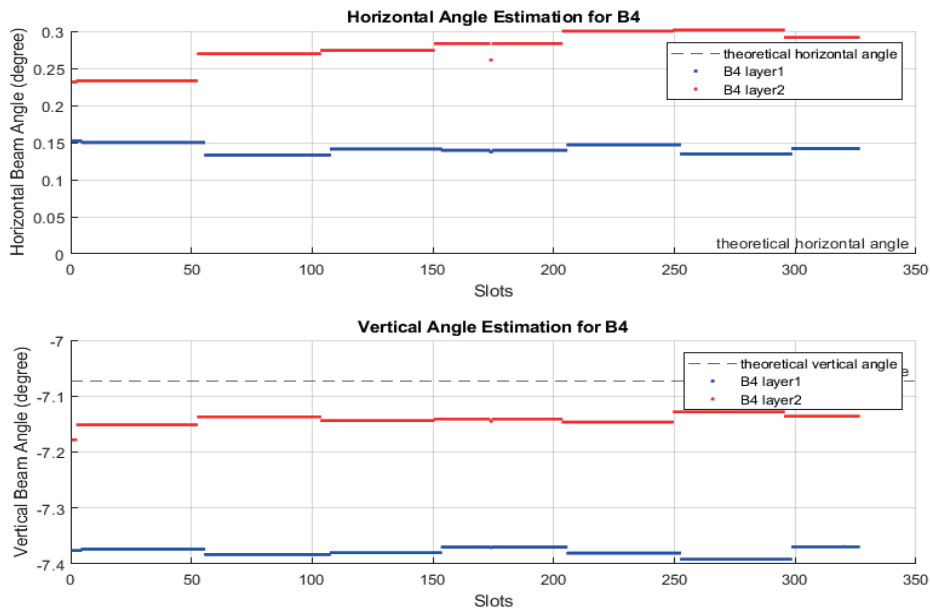
Figure A.17: Peak estimation for B1

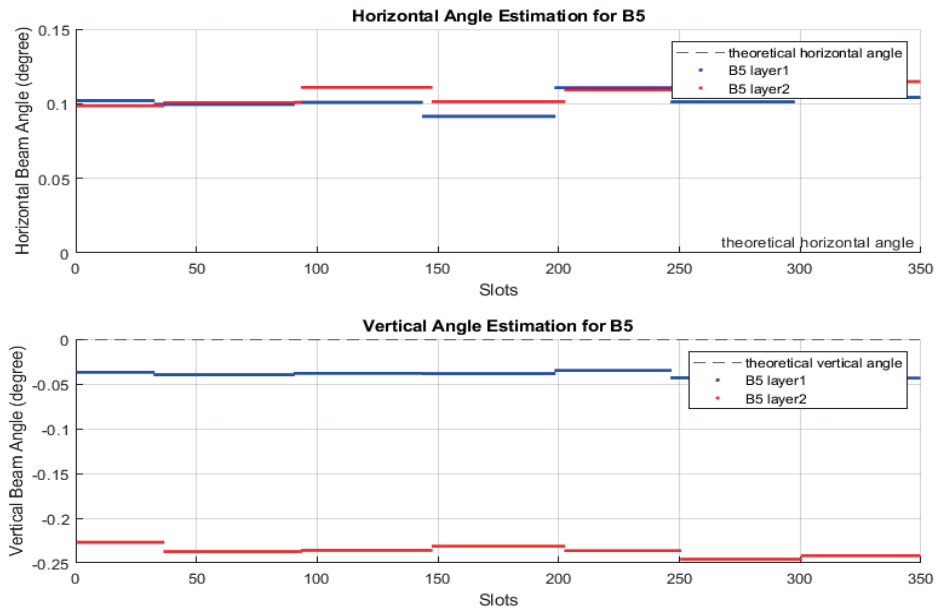**Figure A.18:** Peak estimation for B4

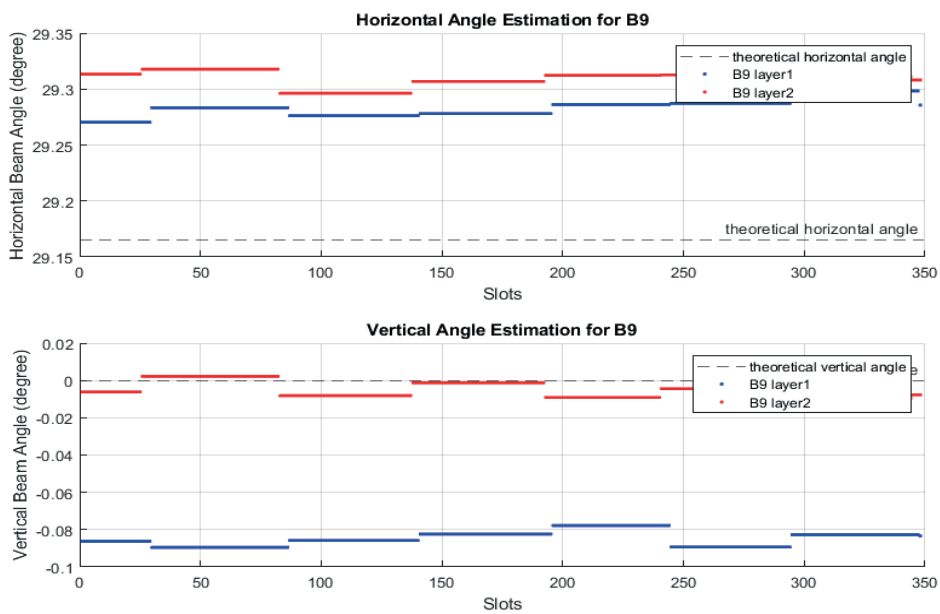**Figure A.19:** Peak estimation for B5

Figure A.20: Peak estimation for B9

A.3 PDSCH measurements for different combinations

Table A.1: PDSCH power measurements for B1, B5, B6, B13

Locations	Throughput	EVM (%rms)	PDSCH (dBm)
boresight	737	3.683	-45.58
left	737	6.636	-45.40
very right	737	5.354	-45.52
up	737	4.650	-45.26

Table A.2: PDSCH power measurements for B1, B2, B5, B13

Locations	Throughput	EVM (%rms)	PDSCH (dBm)
boresight	737	6.739	-45.70
left	737	3.96	-45.29
very right	737	8.159	-45.35
upleft	737	5.422	-45.36

Table A.3: PDSCH power measurements for B1, B6, B9, B13

Locations	Throughput	EVM (%rms)	PDSCH (dBm)
right	737	4.778	-45.40
left	737	3.726	-45.35
very right	737	4.048	-45.39
up	737	5.557	-45.11